Journal of Geochemical Exploration 214 (2020) 106541

Contents lists available at ScienceDirect

Journal of Geochemical Exploration

journal homepage: www.elsevier.com/locate/gexplo

Genesis of the Dounan manganese deposit of southeast Yunnan, China: Constraints from the mineralogy and geochemistry of micronodules

Jianbing Duan[a,b], Yazhou Fu[a,*], Zhengwei Zhang[a], Jiafei Xiao[a], Chengquan Wu[a]

[a] State Key Laboratory of Ore Deposit Geochemistry, Institute of Geochemistry, Chinese Academy of Sciences, Guiyang 550081, China
[b] State Key Laboratory of Nuclear Resources and Environment, East China University of Technology, Nanchang 330013, China

ARTICLE INFO

Keywords:
Dounan Mn deposit
Micronodules
Metallogenetic environment
Ore genesis
Sea level

ABSTRACT

The Dounan manganese deposit in the Middle Triassic Falang Formation has prominent features like oolitic Mn ores, which are in micronodule form. Detailed petrological, mineralogical, and geochemical analyses were carried out on bulk samples and typical micronodules to clarify the deposit's material source, metallogenic environment, genesis, and formation mechanism of the micronodules. The ore minerals are mainly braunite, manganite, Ca-rhodochrosite, kutnahorite, and manganocalcite. The micronodules usually exhibit a detrital nucleus and concentric rings consisting of braunite and Mn carbonate. Good correlations were detected among the Si, Al, Ti, and ΣREE in the ore compositions. The trace elements in the bulk samples and micronodules exhibited similar distribution patterns, and both are enriched in Co, Ni, and Sr and depleted in Cr, Rb, Zr, Nb, Ba, and Th. The micronodules, which are dominated by braunite, are more enriched in V, Co, Ni, Cu, Zn, Mo, and U than the Mn-carbonate-based ones. The ΣREE of the micronodules was higher than that of the bulk samples, but REE patterns were similar. δCe showed weakly positive or negative anomalies, and δEu showed weakly positive anomalies. These results suggest that the ore-forming materials were from various sources, which could have included weathered Mn-bearing rocks from the Yuebei palaeoisland and Emeishan basalts from adjacent ancient lands, as well as a hydrothermal source; mineralisation occurred in a marginal shallow-marine environment with weakly alkaline seawater during fluctuating redox conditions. The micronodules formed via a combination of chemical and biological processes.

1. Introduction

Major metallogenic periods that resulted in the formation of sedimentary Mn deposits in China are the Middle Proterozoic, Nanhua (Neoproterozoic), Ordovician, Devonian, Permian, and Triassic (Fig. 1), of which the Neoproterozoic and Devonian represent the two peak metallogenic periods (Fan and Yang, 1999). No obvious primary metallogenic activities related to Mn have been discovered after the Triassic in China, and thus, the Triassic represents the latest phase of the Chinese marine Mn metallogenic period (Song, 1989). The Dounan Mn deposit, which is located on the western Yangtze platform, occurs in the Middle Triassic Falang Formation and is a typical marine Mn deposit of southeast Yunnan, China (Fig. 2a) (Wu et al., 1994; Huang et al., 1996). Its ore grade is high (average Mn: 20.9%–27.0%) with low levels of impurities (low P, low S, and low Fe). At present, the proven reserves are estimated at 26 million tons (Liu et al., 1984; Li et al., 2009).

In the Dounan Mn deposit, layered Mn oxides and carbonates are associated in the Mn ore bed, and oolitic and pisolitic Mn ores are commonly developed, with many micronodules widely distributed in them (Liu et al., 1984; Hou, 1994). Extensive research has been conducted here, and significant progress has been achieved with respect to understanding the characteristics of the sedimentary facies and the mechanism of metallogenesis of the deposit (Su, 1983; Zhong, 1986; Zheng and Zhang, 1991; Hou, 1994; Liu and Xue, 1999; Li et al., 2009; Xia et al., 2010; Tang and Yi, 2011; Du et al., 2013). However, two core issues remain controversial or unresolved, namely, the genesis of the deposit and the formation mechanism of the micronodules. On the genesis of the ore deposit, Su (1983) and Zhong (1986) proposed that the Mn was derived from the surrounding palaeocontinents and the Dounan Mn deposit represents an ordinary marine sedimentary deposit. However, Liu et al. (1988) and Zheng and Zhang (1991) concluded that Mn was derived from hydrothermal fluids, and mineralisation was controlled by the hydrothermal process. On the other hand, there are only a few studies that focus on the micronodules in the Dounan Mn deposit. Su (1983) suggested that biological effects and Mn enrichment

* Corresponding author.
E-mail address: fuyazhou@mail.gyig.ac.cn (Y. Fu).

https://doi.org/10.1016/j.gexplo.2020.106541
Received 7 August 2019; Received in revised form 19 December 2019; Accepted 28 March 2020
Available online 03 April 2020
0375-6742/

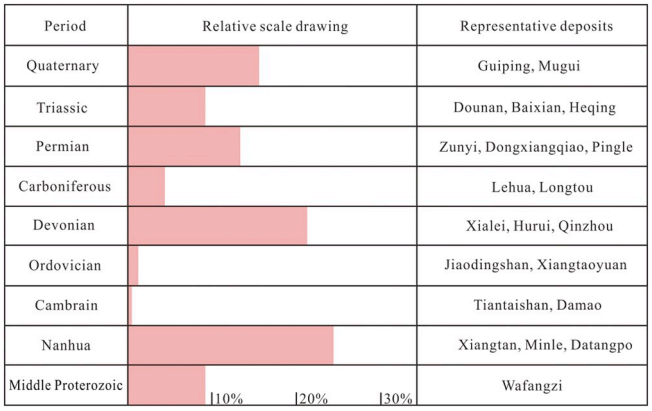

Fig. 1. Temporal distribution of the important Mn deposits in China. [Modified after Fan and Yang, 1999.]

could be closely related; Du et al. (2013) conducted a study on the morphology of micronodules and believed that the metallogenic environment of the deposit was located near a palaeo-redox interface. The manganese nodules both in terrestrial and in the ocean are all important mineral resources. They are usually spherical or ellipsoidal, with nucleus and concentric rings (Su, 1983; Bolton, 1988; Ostwald, 1990; Hein et al., 1997, 2013; Salama et al., 2012; Du et al., 2013; Bau et al., 2014). However, their mineral assemblages, chemical composition, metallogenic backgrounds, and ore-controlling factors are different (Bathurst, 1975; Frakes and Bolton, 1984; Bolton and Frakes, 1985; Usui and Someya, 1997; Hein et al., 2013; Bau et al., 2014). Therefore, it is very necessary to carry out research on micronodules in the terrestrial Mn deposit.

We conducted a systematic study on the mineralogy and geochemistry of bulk samples and micronodules from the Dounan Mn deposit to determine the origin, metallogenic environment, and genesis of the deposit and to elucidate the micronodule formation mechanism. The results obtained in this study will improve our understanding of the similarities and differences in the formation mechanisms of micronodules in ancient marine Mn deposits and of nodules in modern oceans. Furthermore, these results will contribute to studies on the Middle Triassic palaeoceanic environment in South China, including transgression and regression events, and the redox changes in seawater.

2. Geological setting

The study area is part of the western margin of the Yangtze platform in South China (Fig. 2a). On a macro level, the regional topography resembles a 'U', with the study area being surrounded by the Yuebei palaeoisland in the south, Ailaoshan uplift in the south-west, Kangdian palaeocontinent in the west, and Niushoushan palaeoisland in the north (Fig. 2b). Among them, the Yuebei palaeoisland is composed of the Mn-enriched granitic gneiss, biotite schist, and limestone from the Devonian (MnO: ~0.2%) (Guo, 2006); the Ailaoshan uplift is composed of biotite plagioclase gneiss, amphibolite, and other metamorphic rocks (MnO: ~0.2%) (Wang, 2012); the Kangdian palaeocontinent and Niushoushan palaeoisland are mainly composed of iron-manganese slate in the Lower Cambrian Kunyang Group (MnO: ~0.41%) (Yang, 2003). Moreover, the Permian Emeishan basalts are widely distributed on the ancient lands of Yuebei and Kangdian (MnO: ~5.18%) (Liu et al., 1984). The region originated from the Anisian carbonate platform, and under the influence of the Indosinian tectonic movement, the two sides of the Mingsu fault disconnected, rose, and fell away from each other. The side near the Yuebei palaeoisland was raised, forming a beach, whereas the other side sunk and formed the Dounan basin. During the Ladinian Age, due to the stable subsidence and several transgressions in the Dounan basin, more than 800 m thick sedimentary rock series with sedimentary rhythmic cycles were deposited in the basin and formed the Falang Formation, including some Mn-bearing units. The junction of the Mingsu fault and Wenma fault producing the slope of the Dounan basin, was the main area of Mn mineralisation, in which there were many Mn deposits such as Dounan, Laowu and Daqing, as well as a series of Mn ore occurrences. The sedimentary lithologic combination of the Falang Formation in the study area is characterized by different lithofacies during the same period. The main lithological boundary is roughly in the east-west direction on both sides of the Kaiyuan uplift. The area west of the uplift comprises endogenous carbonate rocks dominated by detrital limestone, whereas in the east, including the uplift, the main lithology changes from manganiferous clastic limestone to detrital rock formed by turbidity currents.

Tectonically, the study area is located in the eastern part of the intersection of the Honghe fault and the Shizong-Mile fault (Fig. 2). The subduction of the Yuebei palaeoisland caused the formation of the Kaiyuan uplift, and on both sides of the uplift, formed the Dounan basin and Gejiu basin, respectively. The curved structure formed by the intersection of the northeastern Mingsu fault and the northwestern Wenma fault mainly controls the Mn deposits on the slope of the Dounan basin. The Dounan basin formed against the background of long-term activity of the Mingsu fault and continuous settling of surrounding continental sediments.

The Mn-bearing strata of the Dounan Mn-ore belt belong to the Middle Triassic Falang Formation (T_2f), which forms a conformable contact with the sandy clastic rock of the Upper Triassic Niaoge Formation and an unconformable contact with the limestone of the Middle Triassic Gejiu Formation. The lithology of the Falang Formation comprises a set of shallow-marine mudstone, siltstone and sandstone interbedded with carbonate rocks containing lamellibranchs, brachiopods, gastropods, algae, and other fossils (Liu et al., 1988; Liu and Xue, 1999; Du et al., 2013). This formation is subdivided into six stratigraphic units (T_2f_1–T_2f_6), including two main ore-bearing units (T_2f_4 and T_2f_5) (Fig. 3). The lower ore-bearing unit consists of dark-grey silty mudstone, argillaceous siltstone, grey-green mudstone, and brecciated limestone and Mn ore layers ($T_2f_4^1$). The upper ore unit comprises argillaceous siltstone, sandstone, and Mn ore layers ($T_2f_5^2$; Liu et al., 1988; Zheng et al., 1991; Liu and Xue, 1999).

3. Deposit characteristics

The Dounan Mn deposit ranges from the west of Gake to the east of Xinzhai, where it forms a large syncline with a length of 7.3 km, width of 0.15–2.7 km, and a surface area of approximately 19 km^2 (Fig. 4). Consistent with the characteristics of the ore bodies and the geographical position, the deposit is divided into two main ore-bearing units ($T_2f_5^2$ and $T_2f_4^1$; Fig. 3a) and five ore sections. The Gake ore section is to the west of the syncline, the north limb of the syncline comprises the Kata and Baigu ore sections, and the south limb comprises the Daaozi and Milike sections; among these, the Gaka and Baigu sections are the main industrial ore sections (Fig. 4). There are obvious lithological differences between the eastern and western sections of the deposit; the former is mainly a combination of mudstone and carbonate rocks, and the latter transitions into siltstone and carbonate rocks. The Gake section only contains the lower ore layer ($T_2f_4^1$) (Fig. 3c), whereas the Baigu section only contains the upper ore layer ($T_2f_5^2$) (Fig. 3b).

The ore bodies usually have a stratiform, stratoid, and lenticular morphology. In addition to the separate layers of Mn oxides and carbonates (Fig. 5a, b), a combination of the two types was also noted in the ore bed (Fig. 5c) (Liu et al., 1984; Hou, 1994). The Mn ore types of the different ore blocks are similar and mainly of primary Mn ores (Liu et al., 1984). Consistent with the macroscopic appearance, the Mn ores can be divided into compact massive Mn ores (Fig. 5c, e), oolitic and pisolitic Mn oxide and carbonate ores, and mixed Mn ores. The oolitic and pisolitic Mn oxide ores are mostly black, with grain diameters of 0.5–6.0 mm. Some oolitic grains have been deformed, and when the

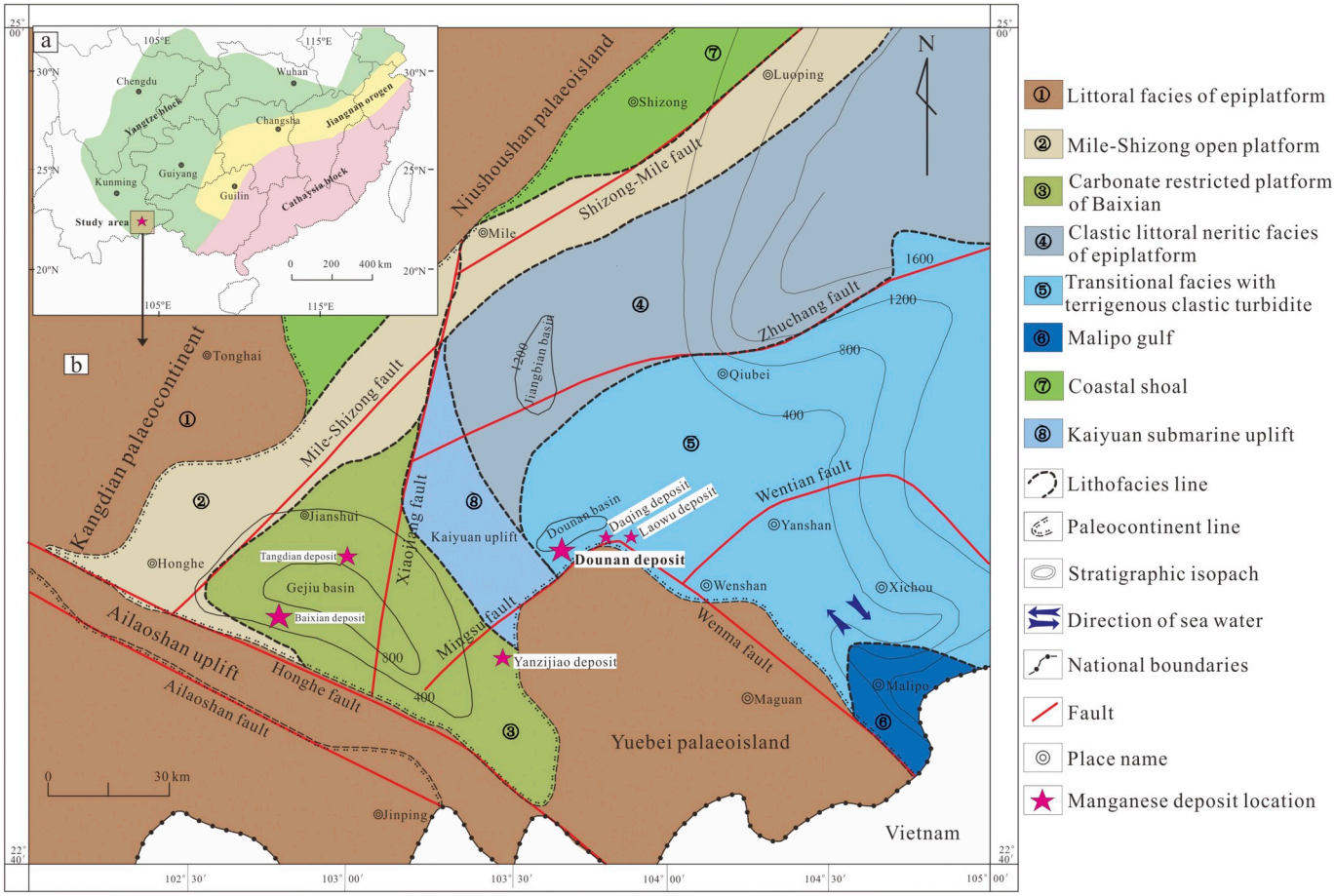

Fig. 2. (a) Tectonic sketch map of South China and the location of the study area [modified after Zhu et al., 2013]; (b) the palaeotectonics and palaeogeography in southeastern Yunnan during the Ladinian [modified after Liu et al. (1984) and Hou et al. (1997)].

ooliths or pisoids are dense, their individual primary shapes become unclear or disappear completely, thereby forming a dense, banded, thin layer interbedded with Mn carbonate ores (Fig. 5h, i). The colour of the oolitic and pisolitic Mn carbonate ores is grey or purple red, with diameters of 0.2–5.0 mm, and these are often cemented with calcite, quartz, feldspar, and dolomite (Fig. 5f). The mixed Mn ores are characterized by the presence of purple-red Mn carbonate ores and black oolitic, pisolitic, clastic, and cloddy Mn oxide ores that often show a slight laminar structure (Fig. 5d, g). Among the mineral textures, the most common is the oolitic texture (Fig. 5j), followed by the microgranular blastic texture of the Mn oxide (Fig. 5k) and the clastic texture that is widely developed in the mixed Mn ores (Fig. 5l). In general, the ore combination of the Dounan Mn deposit is relatively simple, and no ore combination was produced from volcanism or metamorphism.

4. Samples and analytical methods

In the field work, we selected two typical ore sections of Baigu and Gake that can represent the upper and lower ore layers, respectively, and we sampled by going down to the mine. The sampling locations were the fresh profiles of the V_8 ore blocks in the Baigu section (Fig. 3b) and the V_1 ore blocks in the Gake section (Fig. 3c). The selected eight samples were representative Mn oxide and Mn carbonate ores, which were taken by continuous sampling along the vertical profiles. All samples were investigated by employing various petrographical, mineralogical, and geochemical techniques.

The samples were prepared as polished thin sections for petrographic study and analysed under transmitted polarising and reflected light microscopes. The mineralogical analyses were conducted by X-ray powder diffraction (XRD) using a Philips X'Pert diffractometer (Malvern Panalytical B.V., the Netherlands). The analyses were performed at the State Key Laboratory of Ore Deposit Geochemistry, Institute of Geochemistry, Chinese Academy of Sciences (SKLODG, IGCAS, hereafter).

For a detailed investigation of the micromorphology and chemical composition of the different minerals in the polished sections of the samples, we conducted scanning electron microscopy coupled with energy dispersive X-ray spectroscopy (SEM-EDS) using a JSM6460-LV (JEOL, Japan) instrument at SKLODG, IGCAS. The samples were scanned with a focused electron beam produced by a field emission gun (W-crystal) using 20 kV acceleration under high vacuum conditions (10^{-9} mbar). The scanning beam has a diameter between 1 and 5 μm and maximum magnification of 2×10^5 times.

All samples were crushed to 200-mesh size for whole-rock geochemical analyses, and the major and trace elements were analysed at SKLODG, IGCAS. The samples were mixed with $Li_2B_4O_7$ at a ratio of 0.4 g of sample and 8 g of $Li_2B_4O_7$. The major elements were analysed by X-ray fluorescence using a PANalytical Axios instrument (Malvern Panalytical B.V., the Netherlands) following the method documented by Hu (2009). The detection limit for all the major oxides was 0.01 wt%, and the relative analysis errors were less than 3%. The trace elements [including rare earth elements (REEs)] were analysed by inductively coupled plasma-mass spectrometry (ICP-MS) using an ELAN-DRC-e instrument (PerkinElmer, USA) following the method documented by Qi et al. (2000a). The detection limits were as follows: Tb, Ho, Lu, Cs and Tm—0.01 ppm; Er, Eu, Sm, Pr and Yb—0.03 ppm; Ba, Ce, Co, Th, Gd, Dy and U—0.05 ppm; Ta, Nd, Ga and Sr—0.1 ppm; Rb, Cu, Ni, Nb and Hf—0.2 ppm; Y, Pb and La—0.5 ppm; W and Sn—1 ppm; Zr and

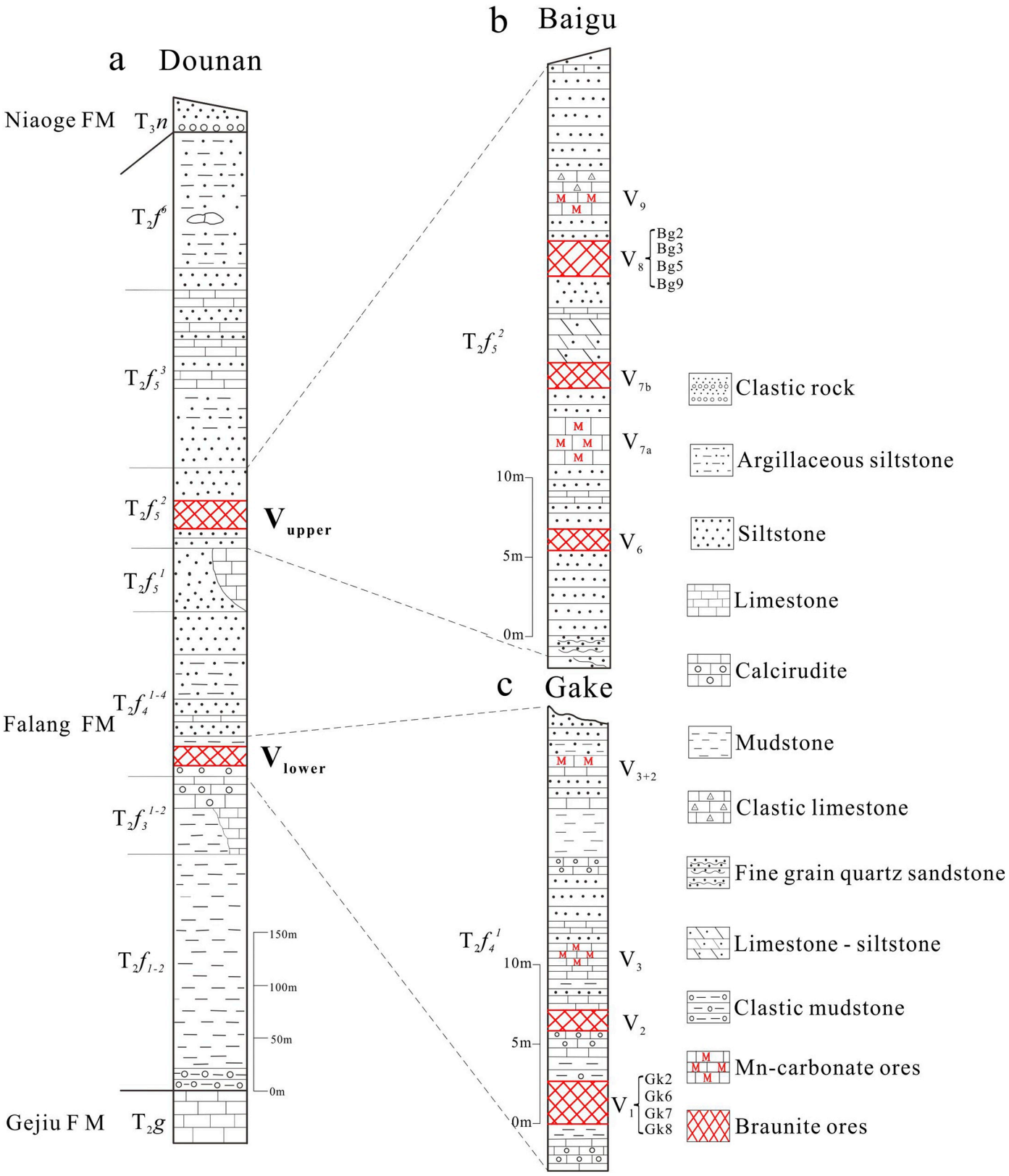

Fig. 3. Stratigraphic column of Dounan Mn deposit. "a" is for the whole ore sections of Dounan Mn deposit "b" and "c" are the stratigraphic columns of upper and lower ore sections for Baigu and Gake.
[Modified after Su, 1983.]

Mo—2 ppm; V—5 ppm; and Cr—10 ppm. The relative analysis errors were less than 10%.

In situ chemical analyses, namely, electron microprobe analyses (EMPA) and laser-ablation ICP-MS (LA-ICP-MS), were performed for two types of oolites (Mn oxide and carbonate ores) in polished sections at SKLODG, IGCAS. The major element concentrations were detected by

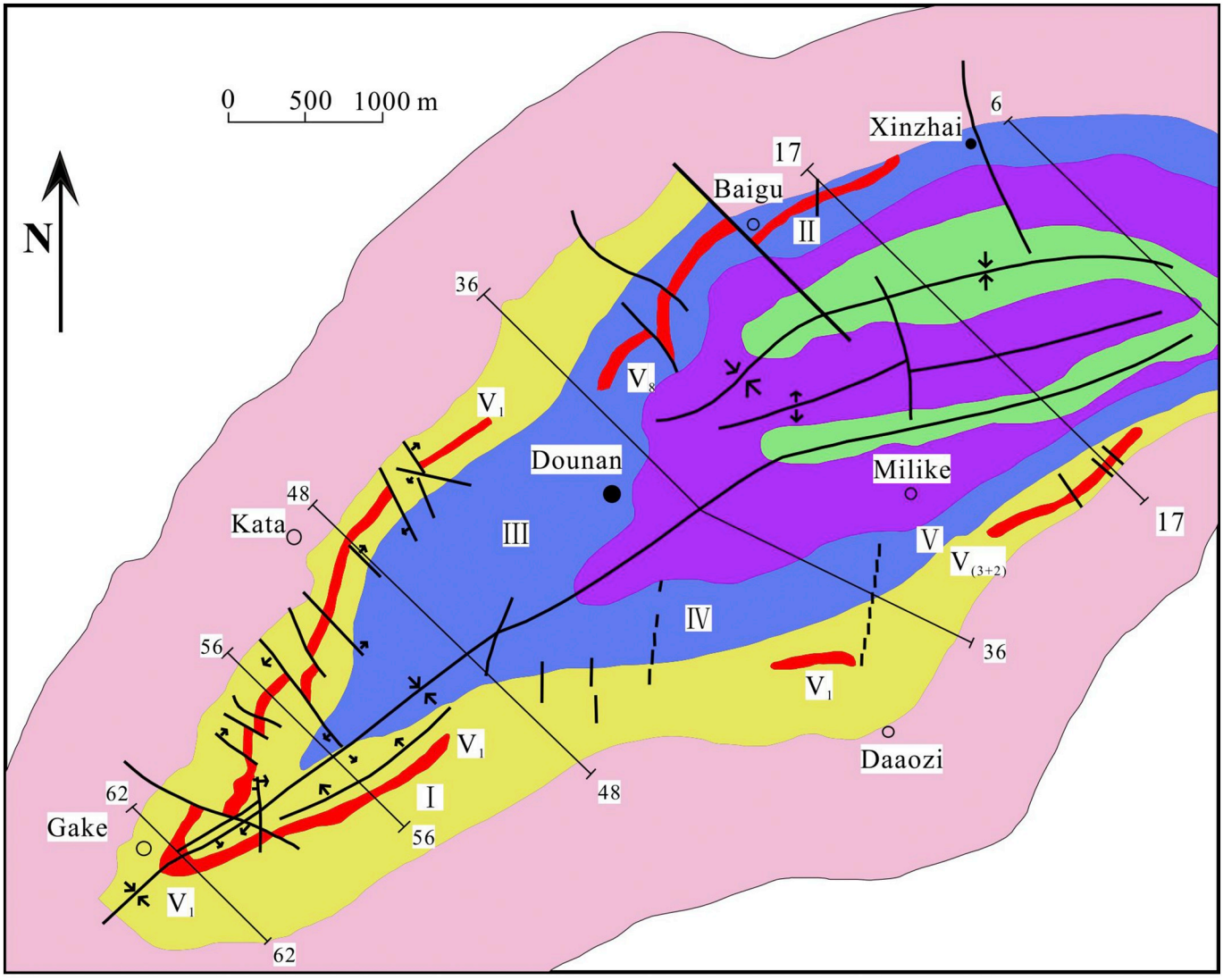

Cross section along prospecting line 56

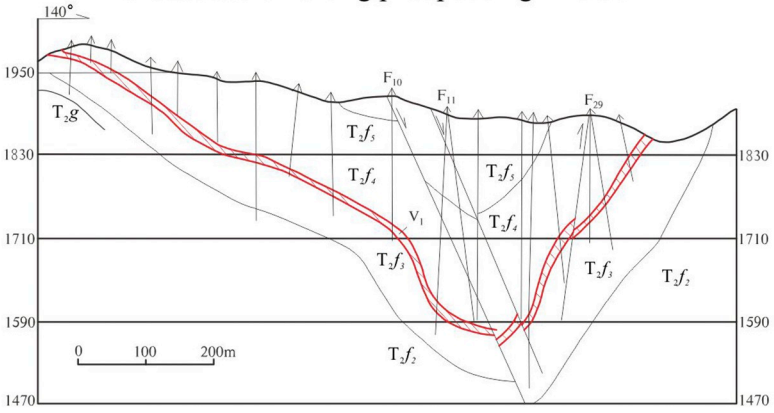

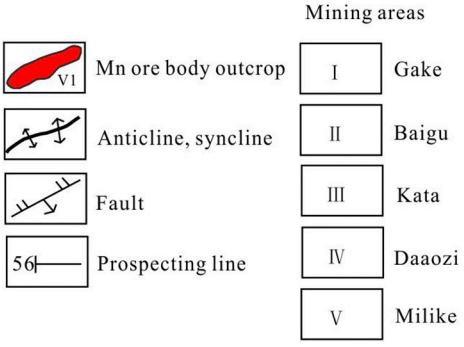

Middle Triassic

Falang Formation

T_2f_6 Mudstone, siltstone

$T_2f_5^2$ Upper Mn formation, mudstone siltstone, sandstone, Mn horizons

$T_2f_4^1$ Lower Mn ore formation, limestone, Mudstone, siltstone, Mn horizons

Upper Triassic

T_3n Niaoge Formation, sandstone, conglomerate

Middle Triassic

T_2g Gejiu Formation, limestone

(caption on next page)

Fig. 4. The Triassic stratigraphic map and typical cross section of the Dounan Mn deposit. [Modified after Liu et al., 1984].

EMPA using a JEOL-1600 instrument (JEOL, Japan) on polished thick sections at 15/20 kV accelerating voltage and 10 nA beam current. The Mn-oxide rich parts and the Mn-carbonate rich parts were both measured with a focused (1–5 μm) beam. All detected points were arranged in a line and the distance between the adjacent points was approximately 100 μm (Fig. 6a, b). The analysed elements were Mn, Fe, Na, Mg, Al, Si, K, Ca, P and Ti. Rhodonite (Mn^{2+}), manganese titanate (Mn^{3+}), haematite (Fe), kaersutite (Mg, Al, Si), albite (Na), biotite (K), apatite (Ca, P) and rutile (Ti) were used as standards (SPI Minerals Standard in the USA and ZBA Oxide Set of CAMECA company in French). The oxides contain significant amounts of water within their crystal structure [manganite ~10–20 wt%; Chukhrov et al., 1979], and

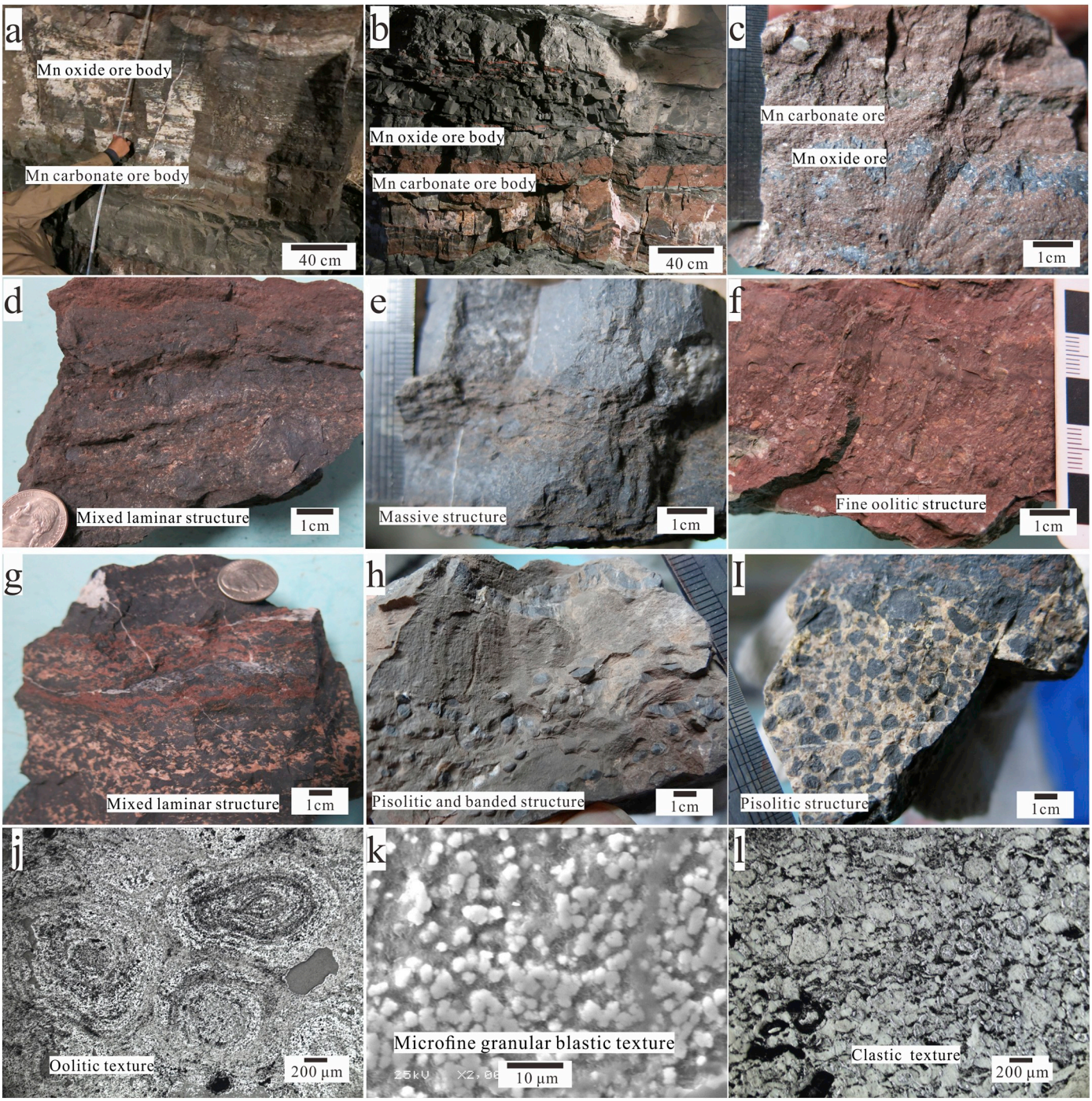

Fig. 5. Mn-bearing rock series, morphology of ore bodies, and structures and textures of ores in the Dounan Mn deposit in southeast Yunnan, China.
a: Mn-bearing rock series in Baigu; b: Mn-bearing rock series in Gake; c: massive structure, Mn oxide ore interbedded with Mn carbonate ore; d: mixed laminar structure; e: massive structure; f: fine oolitic structure, Mn carbonate ore; g: mixed laminar structure; h: pisolitic and banded structure; i: pisolitic structure, Mn oxide ore; j: oolitic texture; k: microfine granular blastic texture; l: clastic texture.

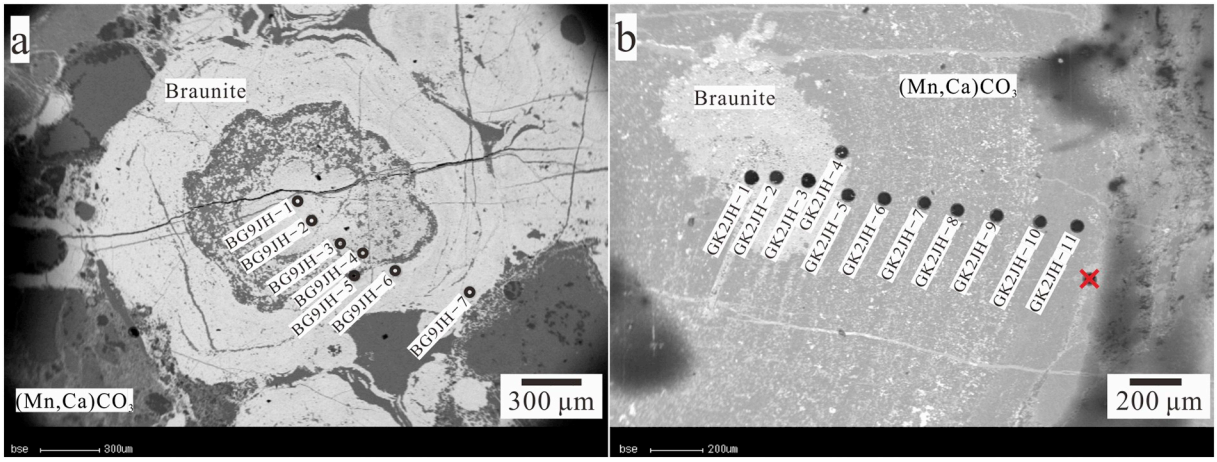

Fig. 6. BSE microphotographs showing LA-ICP-MS and EMPA points analysed of micronodules (a and b) in the Dounan Mn deposit.

the loss on ignition for the whole-rock samples was approximately 20%. As the target elements do not comprise the total composition of the minerals, the analytical sums obtained after EMPA were often well below 100%. Therefore, we choose data that is close to 100% after conversion to oxides, and the unreliable data were omitted from further consideration and discussion. The trace element concentrations of micro-area in the polished sections were determined by LA-ICP-MS, for which the sampling positions were the same as those for EMPA. The detailed operating conditions for the LA system and the ICP-MS instrument and data reduction are the same as those described by Liu et al. (2008). Each analysis incorporated a background acquisition of approximately 20 s (gas blank), followed by 50 s data acquisition from the sample. The element contents were calibrated against the reference materials NIST 610 (USA National Institute of Standards and Technology) and artificial standard sample (the artificial standard sample was made by pressing the powder of the manganese nodule NOD-P-1(USGS), and the homogeneity of this standard was tested by laser ablation), along with application of internal standardisation of the electron microprobe-determined Mn and Si contents. The detailed preparation method and process of the artificial standard sample were described by Qi et al. (2000b). Off-line selection and integration of background and analytical signals, and time-drift correction and quantitative calibration were performed using ICPMS DataCal (Liu et al., 2008).

5. Results

5.1. Petrography

The selected samples were dark grey and purple red in colour with massive, banded, and mixed laminar structures (Fig. 5c, f, h, i). Mn minerals exhibit various forms of oolitic micronodules, with mostly spherical or ellipsoidal shapes and diameters of approximately 0.1–1.0 mm (Fig. 7). Some micronodules have laminar concentric structures (Fig. 7a, b), whereas some layers of the micronodules are unclear or even discontinuous (Fig. 7c, d). The thickness of a single layer is approximately 10–50 μm, and there are approximately ~20 layers in a micronodule with a clear layered structure. Parts of the micronodules have nuclei, usually composed of carbonate rock, quartz, feldspar, biological debris, or other components (Fig. 7b, c). The micronodules can be divided into three categories according to their morphological characteristics—undamaged (Fig. 7a, b), half-damaged (Fig. 7c, d), and modified residual (Fig. 7e, f). The first type is spherical or ellipsoidal with clear bright and dark rings; EDS reveals that the bright rims are mainly braunite ($3Mn_2O_3{\cdot}MnSiO_3$) and the dark ones are Mn carbonate ores. The morphology of the second type indicates that the micronodules were altered by crushing or by cutting of veins; the bright braunite rings are discontinuous or even fragmented, but the outline of the initial micronodules is clearly visible. The initial characteristics in the third type show complete transformation; the light and dark rings disappeared, leaving only the original outline of the primary micronodules, and the type of Mn mineral has been changed.

Two typical micronodules were BG9JH and GK2JH from the Baigu and Gake ore units (Fig. 6). Microscopic observation showed that BG9JH is irregularly spherical, approximately 2 mm in diameter, with unclear layers, fracture features (Fig. 6a), and a deformed edge. The minerals in the central part and the outer rings of BG9JH comprise braunite, and the middle ring mainly consists of Mn Carbonate minerals. GK2JH is ellipsoid, approximately 3 mm in diameter, with unclear layers, and was cut by Mn-bearing calcite veins (Fig. 6b). The minerals of GK2JH mainly comprise Mn carbonate, with a small amount of spot-like braunite in the centre and interlayers.

5.2. Mineralogy

The XRD results showed that the Mn minerals in the bulk samples from the Dounan Mn deposit are mainly composed of braunite, Ca-rhodochrosite, manganocalcite and kutnahorite, and a lesser amount of manganite. The mineral assemblages in the different types of ores showed individual characteristics, for example, the oolitic mineral in Fig. 5h is mainly manganite, the mineral in black in Fig. 5i is braunite, the minerals in the brown part in Fig. 5f are Ca-rhodochrosite and kutnahorite, and the sample in Fig. 5c consists of braunite and kutnahorite.

SEM-EDS analysis showed that the mineral composition of micronodules can be divided into three types: (1) mainly composed of concentric-ring-shaped braunite and containing a small amount of manganite and Mn carbonate minerals, such as BG9JH (Fig. 6a); (2) mainly composed of concentric-ring-shaped Mn carbonates (Ca-rhodochrosite and manganocalcite), together with a small amount of braunite, for instance, GK2JH (Fig. 6b); and (3) composed of braunite and carbonates in the form of concentric rings, with Mn carbonates in manganocalcite and Ca-rhodochrosite (Figs. 7d and 8a). Furthermore, a small volume of debris minerals is mixed with the Mn minerals, including quartz, feldspar and the like. Observations by SEM under high magnification indicate a clear octahedral and hexahedral crystal form in the micronodules (Fig. 8), and those by EDS show that the micronodules comprise braunite (Fig. 8b_1) and manganocalcite (Fig. 8b_2). Parts of the kutnahorite also show growth zoning (Fig. 8c).

Map scanning results of micronodules with bright and dark interphase bands indicate Mn, Ca, Si, Mg and Fe enrichment in a concentric-ring shape (Fig. 9). The Mn ore mineral in the bright rings is mainly

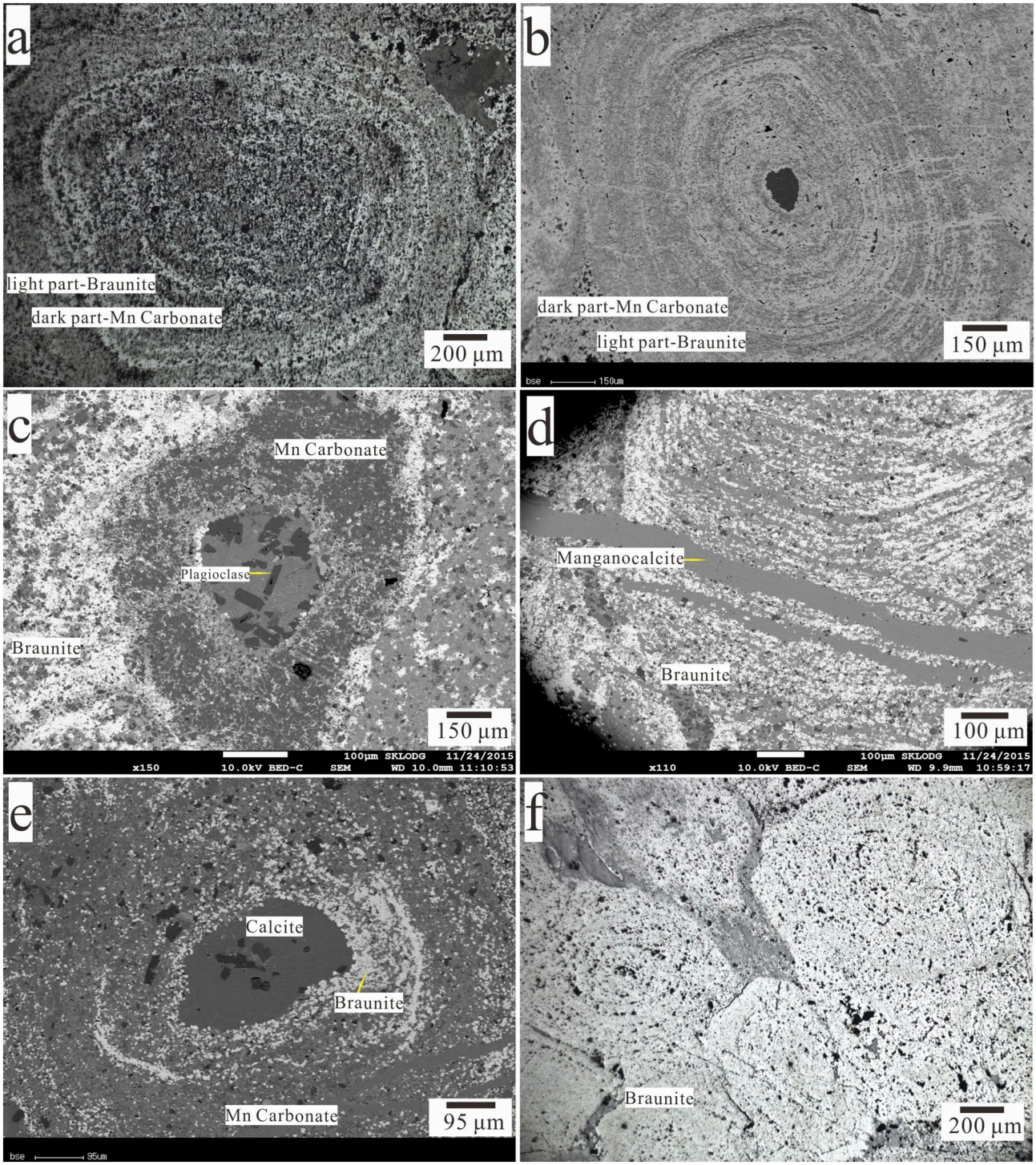

Fig. 7. Different morphologies of micronodules from the Dounan Mn deposit. "a" and "f" were observed using a plane polarised light microscope; "b" and "e" were observed by SEM under back-scattered electron (BSE) mode; "c" and d were observed with EMPA under BSE mode.

braunite and those in the dark rings are Mn carbonates (Ca-rhodochrosite, manganocalcite or kutnahorite). The concentric rings of Fe and the main elements of braunite—Mn and Si—correspond spatially. A similar correspondence is also noted for the concentric rings of Ca, Mg and Mn in the Mn carbonates; however, Mg is concentrated mainly on the edge of the micronodule. Furthermore, the Mn content in the Si-rich ring is much higher than that in the Ca-rich ring.

5.3. Geochemistry

The bulk samples and micronodules from the Dounan Mn deposit have different geochemical characteristics. The major and trace elements and REEs in the eight bulk samples are listed in Table 1. The Mn ores show characteristics of high Mn (mean 20.1%), low Fe (mean 2.1%) and extremely low P and S (both less than 0.1%) contents; the Mn/Fe ratio ranges from 4.95 to 167.5 (mean 54.7). The other major element contents from high to low are Ca, Si, Mg and Ti. The ores, composed mainly of braunite, are relatively enriched in Mn and Si, and

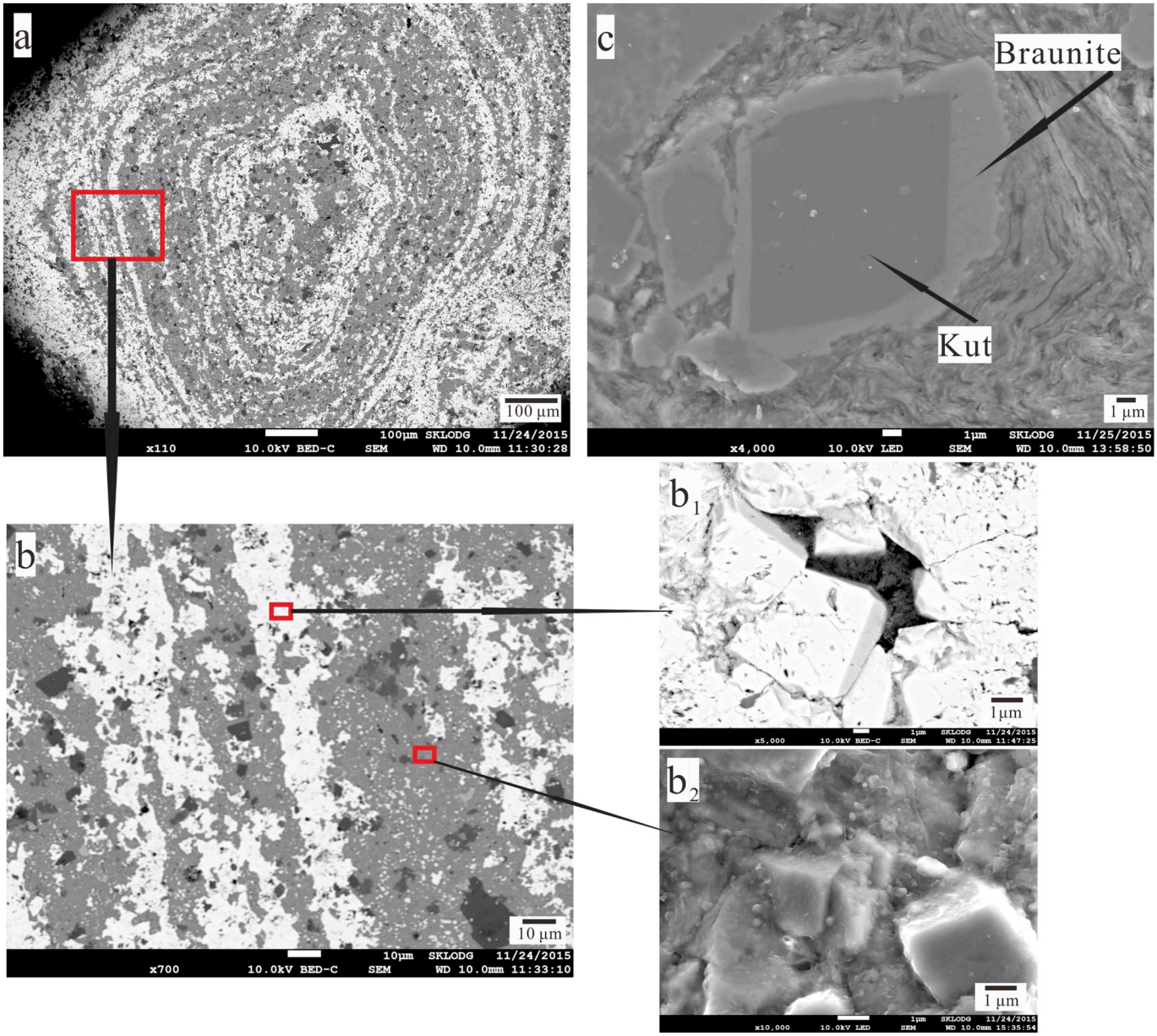

Fig. 8. Crystal form of different minerals under high resolution using SEM-EDS.
a: A typical micronodule with alternating dark and bright rings. b-b_1: Braunite crystal; b-b_2: manganocalcite crystal; c: growth edge of braunite around kutnahorite.

the Mn-carbonate-dominated ores are relatively rich in Mn, Ca and Mg. Compared with average post-Archean Australian shale (PAAS; McLennan, 1989), the bulk samples are enriched in Co, Ni and Sr and depleted in V, Cr, Rb, Y, Zr, Nb, Ba and Th (Fig. 10a_1).

The ΣREE contents of the bulk samples range from 18.0 to 118 ppm (mean 46.0 ppm). The La_N/Yb_N ratio ranges from 0.70 to 0.91 (mean 0.83), showing that the samples are slightly enriched in heavy REE (HREE). The δCe ratio ($\delta Ce = Ce_N/\sqrt{La_N * Pr_N}$) ranges from 0.79 to 1.23 (mean 0.99) and δEu ($\delta Eu = Eu_N/\sqrt{Sm_N * Gd_N}$) ranges from 1.07 to 1.29 (mean 1.17). Ce shows no obvious anomaly characteristics, whereas Eu shows a weakly positive anomaly. The La/Ce ratios range from 0.41 to 0.67 (mean 0.53) and the Y/Ho ratios range from 29.6 to 37.5 (mean 32.9).

The major and trace element and REE compositions of the two micronodules—BG9JH and GK2JH—are shown in Table 2. BG9JH mainly comprises braunite and is relatively rich in Mn, Si, Al and Ti, whereas GK2JH mainly comprises Ca-rhodochrosite, manganocalcite and other components and is relatively rich in Mn, Ca and Mg. In comparison with the trace element concentrations of the PAAS, BG9JH is relatively enriched in Co, Ni, Cu and Sr and relatively depleted in Cr, Rb, Zr, Ba and Th; GK2JH is relatively enriched in Ni and Sr and relatively depleted in V, Cr, Cu, Zr, Nb, Ba, Pb, Th and U (Fig. 10a_2, a_3). Comparison between the two micronodules shows that BG9JH is relatively enriched in V, Co, Ni, Cu, Zn, Mo and U (Table 2). There are significant differences in the REE characteristics of the two micronodules. In BG9JH, the ΣREE concentrations are unusually high at the central points BG9JH-1 and BG9JH-5 (1296 ppm and 2110 ppm, respectively), located at the nuclei and the boundary between the main rings, and those at the rest of the points range between 169 and 291 ppm (mean 229 ppm). The La/Ce ratios range from 0.51 to 0.86, and the Y/Ho ratios range from 29.7 to 42.9 [δCe = 0.82–1.10 (mean 0.90), δEu = 0.85–1.27 (mean 1.10)]. The La_N/Yb_N ratios range between 1.78 and 5.17, showing light REE enrichment. In GK2JH, the points from GK2JH-1 to GK2JH-4 constitute the central part, with braunite being the main ore mineral and with the ΣREE concentrations ranging between 108 and 137 ppm; the ΣREE concentrations of the rest

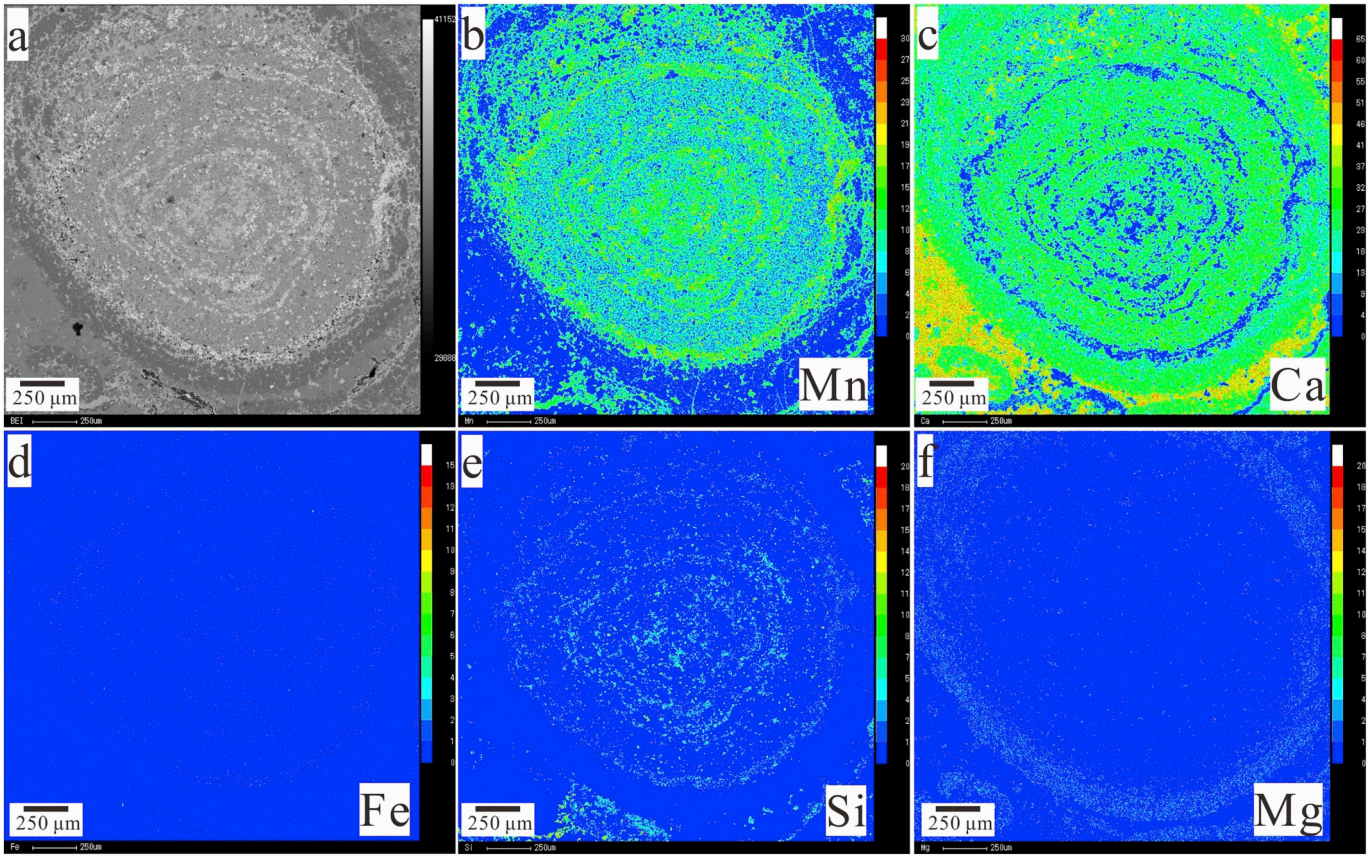

Fig. 9. Mn, Ca, Fe, Si and Mg EPMA mapping distribution for the micronodule GK0. Cool colours indicate low contents; warm colours indicate high contents. We can observe the concentric growth pattern of the layers; Mn, Fe and Si are enriched in the same girdle, the girdle of Ca enrichment shows intergrowth with that of Mn, and Mg is enriched in the outer girdle. (For interpretation of the references to colour in this figure legend, the reader is referred to the web version of this article.)

of the points range between 57.9 and 146 ppm (mean 95.4 ppm, i.e. significantly lower than those of BG9JH). Furthermore, La/Ce = 0.40–0.48, Y/Ho = 32.2–38.5, δCe = 1.18–1.40 (mean 1.28), δEu = 0.75–1.28 (mean 1.08) and La_N/Yb_N = 0.58–0.84, indicating that GK2JH is enriched in HREEs.

6. Discussion

6.1. Source(s) of Mn

Generally, Mn in a deposit could be exogenous or endogenous, or it could be derived from multiple sources. One source of Mn could be terrestrial Mn-containing materials that were enriched in a limited space (basins) and were deposited by sedimentation/diagenesis (Van Houten and Arthur, 1989; Young, 1989a, 1989b; Burkhalter, 1995; Macquaker et al., 1996), and other important sources could be Mn-containing hydrothermal fluids and/or volcanic materials (Nicholson et al., 1997; Öksüz and Okuyucu, 2014).

The relationship between Si, Al, and Ti in sedimentary deposits often provides information on the sources of ore-forming materials. For instance, Al and Ti are the main components of continental crust rocks, soils, and weathering products; their contents in seawater are extremely low (Taylor and McLennan, 1985; Toyoda and Masuda, 1990). Furthermore, Al and Ti enrichment in authigenic sediments by seawater is very low compared with that in sedimentary detrital materials. Therefore, Al and Ti in marine sediments are generally considered to all be derived from terrigenous detrital materials. In addition to debris and clay minerals, Si could be derived from biological processes or hydrothermal fluids (Crerar et al., 1982; Sugisaki, 1984; Shah and Khan, 1999; Brusnitsyn, 2013). In the Dounan Mn deposit, Si, Al and Ti in the bulk samples showed good positive correlations (Table 3), thus indicating that they are homologous and mainly derived from debris. In general, rare earth elements (REEs) are chemically stable and may reflect initial information of the original rock after undergoing weathering and alteration (Henderson, 1984). In our study, we noted that the REEs in the bulk samples from the Dounan Mn deposit exhibited good correlations with Si, Al, and Ti (Table 3), which is suggestive of the input of terrigenous materials during mineralisation. Furthermore, the TiO_2/Al_2O_3 ratio is one of the most useful indicators for the provenance of sedimentary rocks because it remains virtually constant during surface weathering and alterations of rocks (Taylor and McLennan, 1985; Hayashi et al., 1997). Therefore, the relatively low TiO_2/Al_2O_3 ratios in both the bulk samples and micronodules (0.04–0.06 and 0.01–0.45, respectively) may indicate a continental source for the Mn in the studied deposit, given that Mn generally is believed to have leached from a continental source and then migrated to the sedimentary basin of deposition (Chauvel, 1974; Garnit and Bouhlel, 2017).

The PAAS-normalised trace element patterns of the bulk samples were similar to those of the two micronodules (BG9JH and GK2JH; Fig. 10a_2 and a_3, respectively), which indicates that they share the same material source. The bulk samples and micronodules are enriched in Co, Ni, and Sr and depleted in Rb, Cr, Y, Zr, Nb, and Th. With respect to the two micronodules, BG9JH is rich in Co, Cu, Ni, Sr, Mo, and W and GK2JH is rich in Ni, Sr, Mo, and W. The different enrichment characteristics of the trace elements in the two micronodules are caused by differences in their mineral compositions. This is because the Mn oxides and hydroxides are active under hydrogenous conditions and either have a strong adsorption capability or have selective replacement for various cation such as Co^{2+}, Ni^{2+}, and Mo^{3+} (Stumm and Morgan, 1996; Anschutz et al., 2005). The distributions of the trace elements of

Table 1
Major oxides (%), trace and rare earth elements (ppm), and elemental ratios of bulk samples from the Dounan Mn deposit.

	GK2	GK6	GK7	GK8	BG2	BG3	BG5	BG9
Ore type	Laminated ore	Banded ore	Mixed ore	Massive ore	Massive ore	Laminated ore	Laminated ore	Mixed ore
Al_2O_3 (%)	3.10	1.82	1.60	1.86	1.53	1.90	1.28	1.04
CaO	20.8	15.6	17.0	18.5	34.8	21.6	10.3	5.72
FeO	4.37	0.98	0.88	1.22	2.36	4.38	0.51	0.40
K_2O	0.52	0.01	0.01	0.01	0.29	0.29	0.08	0.03
MgO	7.30	1.55	1.48	1.57	4.12	2.10	2.14	1.32
MnO	22.5	50.0	49.9	47.4	11.7	27.1	55.2	67.3
Na_2O	0.37	0.45	0.41	0.53	0.28	0.47	0.18	0.10
P_2O_5	0.21	0.14	0.16	0.18	0.14	0.17	0.17	0.14
SiO_2	11.0	10.9	9.55	10.6	6.73	9.79	11.2	10.2
SO_3	0.07	0.05	0.05	0.01	0.20	0.05	0.03	0.02
TiO_2	0.14	0.09	0.10	0.11	0.07	0.08	0.06	0.04
LOI	26.5	13.4	14.0	15.0	35.6	28.5	13.6	7.50
Total	99.2	99.0	99.1	100	99.1	99.0	99.0	99.0
Mn/Fe	5.11	50.8	56.4	38.6	4.95	6.15	108	168
V (ppm)	68.4	58.0	68.0	47.0	110	47.0	44.0	69.0
Cr	27.5	20.0	10.0	20.0	20.0	10.0	10.0	10.0
Co	38.1	154	141	71.0	17.0	13.0	58.0	87.0
Ni	193	179	139	137	50.0	103	187	206
Cu	32.9	35.0	33.0	21.0	3.00	9.00	41.0	54.0
Zn	59.3	54.0	46.0	53.0	24.0	37.0	61.0	71.0
Rb	26.4	0.60	0.60	0.50	14.0	14.4	4.30	1.80
Sr	463	606	586	637	771	1040	297	131
Y	24.8	9.40	9.00	8.00	12.6	14.10	8.10	6.00
Zr	40.9	29.0	22.0	31.0	26.0	32.0	19.0	13.0
Nb	3.96	2.10	1.50	2.20	1.80	1.70	1.20	0.80
Cs	1.68	0.10	0.09	0.08	0.77	0.64	0.17	0.08
Ba	219	548	127	38.8	78.4	149	84.0	26.8
Pb	22.2	54.0	56.0	50.0	11.0	31.0	58.0	72.0
Th	3.15	1.77	1.43	2.03	1.74	1.93	1.33	0.85
U	2.10	1.83	1.93	1.71	1.83	0.72	2.65	3.67
La	22.0	9.00	7.50	7.40	9.60	8.80	6.60	4.20
Ce	53.7	19.3	14.9	15.0	17.9	17.4	10.3	6.30
Pr	4.63	1.70	1.49	1.49	1.90	2.31	1.29	0.80
Nd	18.5	5.80	5.30	5.00	7.00	8.70	4.80	3.00
Sm	3.77	1.28	1.15	1.15	1.66	2.04	1.12	0.69
Eu	1.00	0.32	0.29	0.29	0.42	0.53	0.24	0.20
Gd	4.21	1.24	1.30	1.26	1.70	2.13	0.99	0.77
Tb	0.69	0.21	0.21	0.21	0.29	0.35	0.19	0.13
Dy	4.15	1.32	1.12	1.21	1.56	1.81	1.01	0.71
Ho	0.84	0.29	0.28	0.26	0.37	0.43	0.24	0.16
Er	2.16	0.79	0.75	0.75	1.00	0.98	0.64	0.43
Tm	0.33	0.12	0.13	0.13	0.14	0.17	0.11	0.07
Yb	1.94	0.73	0.66	0.70	0.81	0.78	0.57	0.44
Lu	0.27	0.11	0.12	0.10	0.14	0.14	0.08	0.06
ΣREE	118	42.2	35.2	35.0	44.5	46.6	28.2	18.0
δEu	1.18	1.20	1.12	1.13	1.18	1.20	1.07	1.29
δCe	1.23	1.14	1.03	1.04	0.97	0.89	0.81	0.79
$V/(V + Ni)_{auth}$	0.20	0.20	0.20	0.30	0.23	0.16	0.69	0.25
Ni/Co_{auth}	5.22	1.88	1.13	0.95	2.35	3.22	2.87	8.78
La/Ce	0.41	0.47	0.50	0.49	0.54	0.51	0.64	0.67
Y/Ho	29.6	32.4	32.1	30.8	34.1	32.8	33.8	37.5
La_N/Yb_N	0.84	0.91	0.84	0.78	0.87	0.83	0.85	0.70

the slate in the Kunyang Group of the Kangdian palaeocontinent, the Mn-bearing granitic gneiss, biotite schist and limestone of the Yuebei palaeoisland, and the Permian Emeishan basalts, which are located around the Dounan Mn deposit, are shown in Fig. 10a$_1$. Most of the elements (such as Co, Ni, Zn, Rb, Sr, Th, and U) of the deposit show characteristics similar to those of the Permian Emeishan basalts. Though the V, Cr, Y, Zr, and Nb contents in the deposit are less than those in the basalts, they share the same patterns. This is probably because the Emeishan basalts were weathered and eroded before mineralisation occurred, and these elements were rarely added during the mineralisation process because of their inactive chemical properties.

The PAAS-normalised REE patterns of the bulk samples were similar to those of BG9JH and GK2JH (Fig. 10b), further indicating similarity in their origin. The ΣREE content of BG9JH was higher than that of GK2JH, whereas that of the bulk samples was the lowest. This result could be ascribed to the differences in the type and content of the Mn minerals contained in these samples, for example, BG9JH contains the largest amount of braunite and therefore yields a higher ΣREE content. The ΣREE contents of points GK2JH-1 to GK2JH-4 are significantly higher than those of the other points, which comprise mainly Mn carbonates (Table 2). The relationship between the Mn mineral types and the ΣREE content implies that the ores in this deposit were gradually enriched in REEs by adsorption and/or ion exchange during the oxidation of Mn to form Mn oxides and hydroxides (Usui and Someya, 1997; Surya Prakash et al., 2012). Fig. 10b shows a comparison of the distribution characteristics of REEs between the Dounan Mn deposit and the main rocks of the surrounding ancient lands and Permian Emeishan basalts. The ΣREE contents of the bulk samples from the Dounan deposit were lower than those of the surrounding ancient lands and the Emeishan basalts, whereas the ΣREE contents of the two micronodules were close to those of the surrounding source regions. In the distribution model, the REE patterns of the bulk samples, BG9JH and

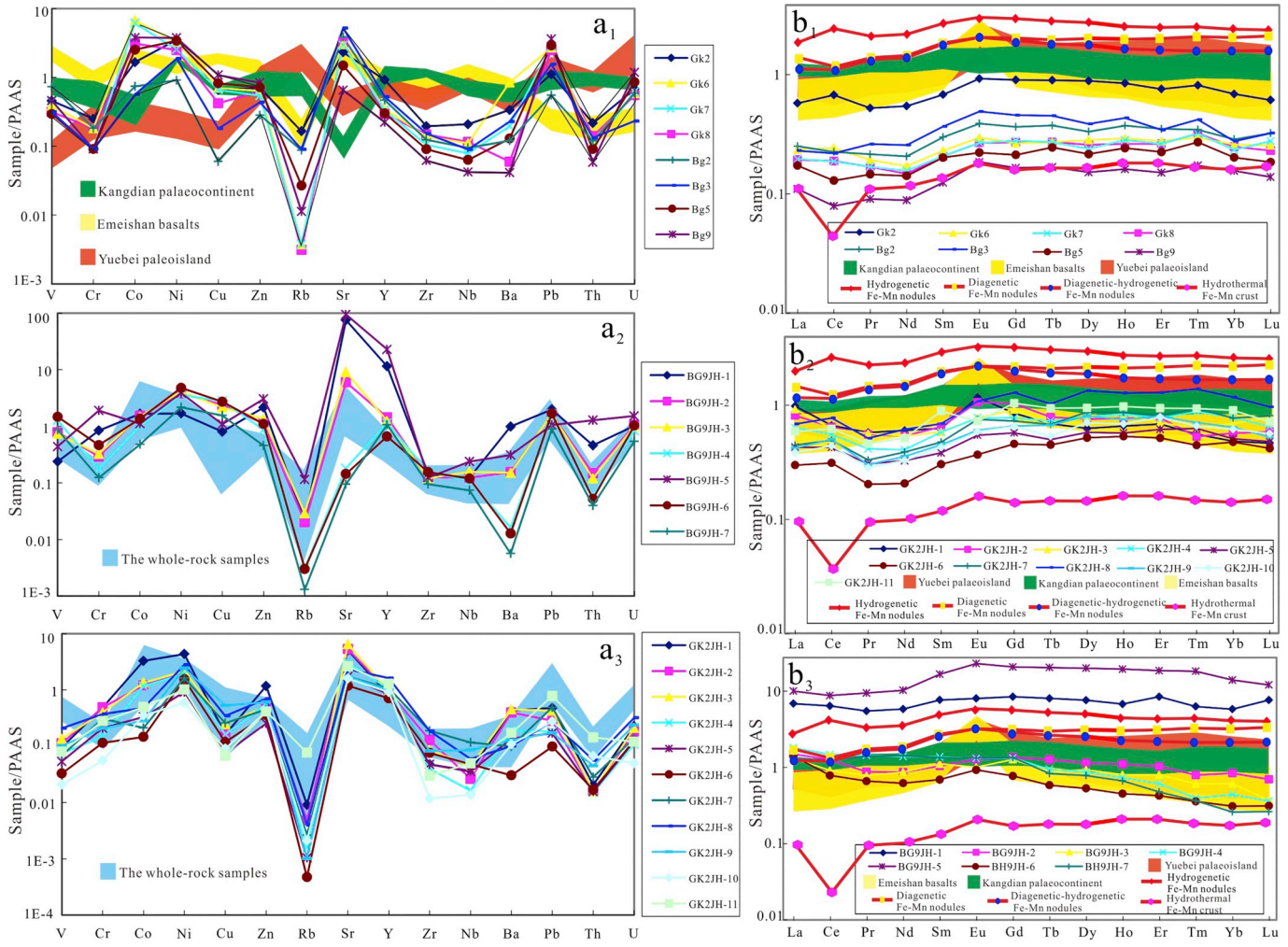

Fig. 10. (a) Spider diagrams of trace elements for bulk samples and micronodules from the Dounan Mn deposit compared with trace elements from different source regions; (b) PAAS-normalised REE patterns of bulk samples and micronodules from the Dounan Mn deposit compared with those of diagenetic, hydrothermal, hydrogenous and mixed type Fe-Mn precipitates [after Bau et al., 2014]. The data for the slate of Cambrian Kunyang Group of Kangdian palaeocontinent, the granitic gneiss, biotite schist and limestone of Yuebei palaeoisland and the Permian Emeishan basalts and were taken from Ji et al. (2016), Guo (2006) and Wang et al. (2007), respectively.

GK2JH exhibited relatively gentle slopes, and the samples were slightly enriched in HREEs; the δCe anomaly was not obvious, whereas δEu showed a weakly positive anomaly. This is similar to the REE distribution patterns of the Permian Emeishan basalts and the rocks of the Yuebei palaeoisland, which indicates that the two kinds of rocks were the major sources of ore-forming material for the Dounan Mn deposit.

The La/Ce ratio of a hydrothermal Mn deposit was found to be close to the seawater value (~2.8), whereas it is much lower (~0.25) in the hydrogenous Mn-Fe crust (Nath et al., 1997). Our results show that the La/Ce ratios of the ores and micronodules from the Dounan Mn deposit range from 0.40 to 0.86 (mean 0.55); that is, the deposit is located between a hydrogenous and hydrothermal Mn deposit but is closer to the former, thus indicating that the Dounan Mn deposit was supplemented with some Mn from a hydrothermal source. The Y/Ho ratios also revealed useful information on the origin of a deposit. The behaviour of Y and Ho is similar; however, Y^{3+} is not as active as other trivalent REEs in fluid and therefore fractionates with Ho^{3+} (Bau et al., 1997; Bau and Dulski, 1999). Furthermore, Y is a high field strength element and is often associated with terrestrial matter; therefore, it is often used to distinguish the source of debris (Maynard, 2010). The Y/Ho ratio of seawater ranges from 44 to 47 (Bau et al., 1996), whereas that of the continental crust and most igneous rocks ranges from 25 to 28 (McLennan, 1989), and that of hydrothermal fluid ranges from 26 to 27 (Pack et al., 2007; Sugahara et al., 2010). In this study, the Y/Ho ratios of the bulk samples, BG9JH, and GK2JH from the Dounan Mn deposit were noted to range from 29.6 to 37.5, 29.7 to 38.5, and 29.7 to 42.9, respectively, thus indicating that the ore-forming material was derived from multiple sources.

In summary, the Mn in the Dounan Mn deposit was derived from multiple sources. The terrigenous materials included the weathering products of the Permian Emeishan basalts and the Mn-bearing rocks of Yuebei palaeoisland were the main Mn source of this deposit, with hydrothermal fluids providing partial Mn supplements.

6.2. Depositional environment

The sedimentary environment is an important factor when studying the mineralisation mechanism of Mn deposits. The palaeogeographic features, petrographic characteristics of the ore-bearing layers, and the physical and chemical conditions of Mn precipitation are the key environmental factors controlling Mn mineralisation.

In regard to the sedimentary environment of the Dounan Mn deposit, Duan et al. (2019) conducted detailed research from palaeogeographic, petrographic, mineralogical, geochemical, and Mössbauer spectroscopic characteristics. Palaeogeographically, the deposit is located in the Dounan basin (Fig. 2), which could have received the

Table 2
Major elements (%), trace and rare earth elements (ppm) and elemental ratios of representative micronodules from the Dounan Mn deposit.

	GK2JH-1	GK2JH-2	GK2JH-3	GK2JH-4	GK2JH-5	GK2JH-6	GK2JH-7	GK2JH-8	GK2JH-9	GK2JH-10	GK2JH-11	BG9JH-1	BG9JH-2	BG9JH-3	BG9JH-4	BG9JH-5	BG9JH-6	BG9JH-7
Na_2O (%)	0.07	0.09	0.04	0.14	0.03	0.10	0.08	0.01	0.03	0.06	0.05	0.07	0.03	0.26	0.04	2.33	0.07	0.03
MgO	2.19	1.89	2.11	1.99	14.5	13.1	9.12	13.7	14.7	12.7	13.5	0.10	0.47	0.61	0.18	0.21	0.16	0.08
Al_2O_3	0.22	0.23	0.04	0.03	0.02	0.01	0.67	0.01	0.03	1.30	1.67	0.70	1.05	0.99	0.71	3.86	0.68	0.53
SiO_2	1.60	1.43	1.09	0.97	0.06	0.22	1.35	0.22	0.16	2.10	3.10	8.91	9.39	8.85	8.71	12.0	9.72	8.78
P_2O_5	0.04	0.04	0.06	0.05	0.05	0.07	0.12	0.07	0.07	0.09	0.07	0.05	0.06	0.11	0.17	0.65	0.11	0.09
CaO	12.5	16.8	21.3	18.7	32.9	31.1	29.3	31.1	32.9	29.2	28.7	1.53	1.11	7.85	1.09	23.6	1.06	2.02
MnO	39.2	32.8	32.1	34.8	7.53	8.50	16.6	10.7	7.85	10.3	8.00	74.9	74.5	64.1	73.6	34.7	76.0	74.3
FeO	1.52	4.75	1.12	1.11	0.08	0.23	0.32	0.26	0.20	1.19	0.49	0.31	0.30	0.49	0.61	0.35	0.28	0.58
Ti (ppm)	33.2	21.5	39.5	17.4	25.5	26.8	108	65.1	76.3	56.0	187	56.8	258	239	327	1054	263	148.9
V	14.4	16.7	20.3	11.2	8.03	4.91	10.3	31.3	15.3	3.12	12.0	35.6	117	111	190	65.7	220	131
Cr	53.5	53.9	43.9	16.3	23.0	12.6	34.1	40.9	23.0	6.12	30.5	92.5	32.2	35.5	19.4	209	51.0	13.6
Co	75.3	27.6	31.0	26.9	7.61	3.36	4.85	11.0	6.51	8.07	11.4	38.2	35.1	34.1	23.0	25.5	31.2	11.02
Ni	238	108	119	107	50.1	84.9	89.5	154	134	32.35	55.6	92.7	211	226	198	213	262	119
Cu	8.08	8.27	12.3	8.08	3.73	5.92	12.8	17.2	26.4	4.53	3.39	40.1	120	108	140	54.6	135.7	77.5
Zn	99.9	47.9	43.7	47.9	21.6	30.5	38.2	59.3	51.5	35.3	35.2	183	95.6	115	73.6	258	93.5	38.6
Rb	1.45	0.77	0.34	0.25	0.17	0.08	0.42	0.64	0.16	0.33	12.3	3.45	3.24	4.61	0.50	18.4	0.48	0.21
Sr	1006	1063	1290	610	345	237	343	468	341	319	523	15,073	1197	1827	36.2	18,894	28.8	18.9
Y	21.9	25.2	25.6	28.1	22.6	19.1	28.6	43.5	27.0	24.7	34. 6	310	38.7	33.5	30.9	617	17.9	28.7
Zr	9.94	26.9	18.0	8.35	9.99	15.9	39.4	39.1	17.3	2.48	6.26	29.8	26.4	25.2	32.6	26.1	32.6	19.9
Nb	0.69	0.50	0.83	0.31	0.67	0.91	2.22	1.13	1.62	0.26	0.94	2.34	2.34	2.98	2.08	4.51	2.26	1.41
Mo	8.82	8.56	8.76	5.20	3.91	2.07	5.44	7.11	3.79	2.03	4.04	10.5	17.9	24.6	12.3	16.7	18.7	7.07
Cs	0.67	0.54	0.18	0.17	0.08	0.01	0.33	0.38	0.02	0.05	1.05	1.25	0.23	0.36	0.14	1.89	0.17	0.01
Ba	281	258	293	124	88.6	19.7	64.4	65.6	83.1	70.2	112	643	101	97.7	10.6	202	8.31	3.67
Hf	0.93	0.79	0.42	0.41	0.22	0.29	0.48	0.57	0.46	0.08	0.59	0.10	1.49	2.54	0.69	22.5	2.31	0.32
W	38.8	26.7	33.0	15.6	17.6	5.35	21.0	40.6	15.3	1.60	6.16	17.7	52.7	54.7	48.7	16.4	65.10	27.8
Pb	9.53	5.66	8.56	3.66	3.40	1.97	9.78	5.51	3.48	5.49	15.6	39.6	32.9	33.1	33.4	21.0	33.7	17.8
Th	0.30	0.23	0.23	0.22	0.23	0.25	0.41	0.82	0.66	0.98	2.08	6.73	2.15	1.75	0.87	18.7	0.76	0.58
U	0.70	0.57	0.65	0.34	0.38	0.39	0.43	0.99	0.74	0.15	0.37	3.15	3.24	3.11	2.60	4.72	3.18	1.67
La	38.9	32.2	36.4	25.2	17.0	11.9	17.7	27.1	16.7	15.3	23.3	282	61.6	53.8	74.2	412	57.7	55.4
Ce	54.9	53.2	51.2	45.8	35.3	25.8	40.7	63.8	41.4	36.3	51.4	549	108	78.4	127	751	67.4	104
Pr	5.28	5.08	5.18	3.81	2.81	1.87	3.04	4.70	2.77	2.60	4.22	52.1	8.31	7.44	13.7	89.9	6.29	13.43
Nd	21.1	18.9	18.9	14.3	11.5	7.27	13.7	21.6	12.5	11.6	18.1	213	31.6	31.6	50.7	375	22.7	52.2
Sm	3.60	3.73	3.37	3.35	2.21	1.75	2.74	3.97	2.60	2.47	5.11	45.9	6.23	6.65	8.19	99.6	4.14	8.03
Eu	1.31	1.19	0.87	0.87	0.61	0.41	0.84	1.22	0.68	0.66	0.81	9.33	1.48	1.17	1.53	26.8	1.08	1.53
Gd	4.11	4.99	4.41	3.75	2.77	2.22	3.51	6.22	3.18	3.15	5.03	42.5	6.77	6.38	6.66	104	3.88	6.77
Tb	0.55	0.63	0.55	0.58	0.40	0.36	0.55	0.83	0.54	0.43	0.75	6.70	1.06	0.74	0.79	17.0	0.49	0.69
Dy	3.04	3.65	3.83	3.85	2.80	2.52	4.23	6.49	3.90	3.41	4.60	38.4	5.76	4.68	4.38	101	2.67	3.94
Ho	0.68	0.79	0.86	0.86	0.59	0.55	0.89	1.31	0.77	0.70	1.00	7.22	1.18	0.86	0.78	20.7	0.48	0.71
Er	2.02	2.29	2.07	2.28	1.82	1.53	2.43	3.81	2.37	2.32	2.79	26.0	3.17	2.46	1.87	57.1	1.31	1.46
Tm	0.23	0.22	0.27	0.37	0.26	0.19	0.39	0.58	0.30	0.28	0.39	2.75	0.35	0.27	0.17	7.97	0.16	0.16
Yb	1.41	1.66	2.01	2.29	1.49	1.39	2.25	3.43	1.88	1.80	2.64	17.6	2.55	1.86	1.34	42.6	0.94	0.79
Lu	0.21	0.26	0.35	0.29	0.22	0.19	0.36	0.43	0.24	0.25	0.32	3.57	0.32	0.17	0.17	5.63	0.15	0.12
ΣREE	137	129	130	108	79.7	57.9	93.3	146	89.9	81.2	121	1296	238	197	291	2110	169	249
δEu	1.60	1.30	1.06	1.15	1.17	0.99	1.28	1.15	1.11	1.11	0.75	1.00	1.07	0.85	0.97	1.24	1.27	0.98
δCe	0.88	0.96	0.86	1.08	1.18	1.26	1.28	1.30	1.40	1.33	1.20	1.05	1.10	0.90	0.92	0.90	0.82	0.88
La/Ce	0.71	0.61	0.71	0.55	0.48	0.46	0.44	0.43	0.40	0.42	0.45	0.51	0.57	0.69	0.59	0.55	0.86	0.53
Y/Ho	32.4	31.8	29.7	32.8	38.5	34.8	32.2	33.2	35.0	35.1	34.5	42.9	32.8	39.15	39.5	29.7	37.1	40.5
La_N/Yb_N	2.03	1.43	1.34	0.81	0.84	0.63	0.58	0.58	0.66	0.63	0.65	1.18	1.78	2.14	4.09	0.71	4.52	5.17

Table 3
Pearson product correlation coefficients between major and trace elements of the whole-rock samples (n = 27).

	MgO	Al_2O_3	SiO_2	CaO	FeO	MnO	TiO_2	V	Cr	Co	Ni	Cu	Zn	Pb	Th	U	ΣREE
MgO	1.00																
Al_2O_3	0.21	1.00															
SiO_2	0.10	0.98	1.00														
CaO	0.35	−0.59	−0.63	1.00													
FeO	0.66	0.58	0.52	−0.04	1.00												
MnO	−0.61	−0.77	−0.72	−0.03	−0.76	1.00											
TiO_2	0.20	0.99	0.99	−0.59	0.59	−0.77	1.00										
V	0.05	0.78	0.72	−0.54	0.29	−0.47	0.74	1.00									
Cr	0.25	0.97	0.95	−0.60	0.62	−0.74	0.97	0.77	1.00								
Co	−0.28	0.11	0.08	−0.43	−0.11	0.28	0.10	0.43	0.19	1.00							
Ni	−0.36	0.23	0.26	−0.65	−0.04	0.26	0.22	0.39	0.26	0.55	1.00						
Cu	−0.31	0.34	0.37	−0.67	−0.13	0.14	0.33	0.55	0.42	0.67	0.54	1.00					
Zn	0.03	0.89	0.87	−0.80	0.41	−0.46	0.87	0.80	0.87	0.35	0.51	0.52	1.00				
Pb	−0.40	−0.45	−0.41	−0.06	−0.35	0.63	−0.44	−0.32	−0.39	0.41	0.21	0.24	−0.29	1.00			
Th	0.23	0.99	0.98	−0.57	0.61	−0.78	0.99	0.74	0.97	0.09	0.19	0.32	0.88	−0.45	1.00		
U	−0.09	0.69	0.69	−0.64	0.15	−0.31	0.67	0.84	0.74	0.49	0.45	0.83	0.73	−0.16	0.66	1.00	
ΣREE	0.53	0.88	0.85	−0.36	0.80	−0.85	0.89	0.57	0.90	−0.02	0.10	0.18	0.70	−0.52	0.89	0.51	1.00

weathered Mn-rich sediments from the surrounding palaeocontinents. Petrographically, the ore-bearing lithology and the sedimentary structures are dominated by horizontal bedding, and the low-angle cross-bedding and graded bedding indicate that the depositional conditions were mainly shallow marine, with relatively agitated water. Mineralogically, there are almost no primary Mn oxides with Mn^{4+}, and the valences of the Mn minerals are Mn^{3+} and Mn^{2+}. Mn minerals of manganite and Mn carbonates are usually deposited under weakly oxidising alkaline conditions and weakly reducing alkaline conditions, respectively (Krauskopf, 1979; Roy, 2006, Fig. 11). From the bottom to the top in the ore profiles of Baigu and Gake, the Mn ores change from braunite to Mn carbonates in a mineral change cycle, and the two types of Mn minerals are often mixed in the middle of the ore beds to form mixed Mn ores (Fig. 3). This implies that the redox condition fluctuated during mineralisation, and the metallogenic process occurred near the redox interface. The cyclical rise and fall of the sea level led to fluctuations in the redox interface. Geochemically, the ratios of $V/(V + Ni)_{auth}$, Ni/Co_{auth}, δCe, and REE distribution pattern of the bulk samples revealed that the Mn deposit formed in an oxidation-dominated depositional environment, with the oxidation properties of different ore beds fluctuating, and small portions of the ore beds formed in weakly reducing environments. The use of Fe^{57} Mössbauer spectroscopic data in research on the sedimentary environment also yielded a consistent result with the geochemical analysis.

The micronodules are commonly developed in the Dounan Mn deposit and represent one of the most typical structures. The tiny size and textural features of concentric rings and nuclei noted in the micronodules strongly indicate that they were authigenic and formed in relatively shallow, agitated water. The main mineral compositions of micronodules are braunite and Mn-carbonate minerals, which formed interphase mineral layers (Fig. 9). This phenomenon indicates that the redox state of the metallogenic medium alternately changed during the formation of micronodules; and the ore-forming environment was weakly oxidised–weakly reduced.

Moreover, the presence of biological fossils such as lamellibranchs, gastropods, bacteria, and algae along with their fragments and the absence of gypsum (which indicates an arid climate) in the ore layer suggest that the Dounan Mn deposit formed under warm weather and normal salinity conditions of a continental margin in a shallow-marine environment (Su, 1983).

Given the above, the metallogenic environment of the Dounan Mn deposit was a shallow-marine basin with normal salinity, and it was near the continental margin; the physicochemical condition for ore formation was weakly alkaline, and fluctuations occurred among oxic, suboxic, and weakly reducing conditions. Changes in the sea level controlled the rise and fall of the redox interface, thereby controlling the formation of Mn ores in this deposit.

6.3. Formation mechanism of micronodules

Nodules are a common form in which Mn ores occur on the modern seabed and in weathered soils. Studies have found that the genetic types of Mn nodules on the seabed are hydrogenetic, diagenetic, hydrogenetic–diagenetic, hydrothermal, or biogenic (Hein et al., 2013; Wegorzewski and Kuhn, 2014). The Mn nodules in soil are considered to be products of secondary oxidation of primary Mn minerals that were formed by free rolling on the surface (Liu et al., 1989; Tan et al., 2000; Peng et al., 2011). However, micronodules in terrestrial Mn deposits differ from the Mn nodules in the ocean and soil in terms of size, mineral types, and their formation mechanism is supposedly dominated by microbial action (Ehrlich, 1980; Janin and Bignot, 1983; Krumbein, 1983; Ostwald, 1990).

In accordance with the analyses of the present study of the source and metallogenic environment, the forming mechanism of the micronodules in the Dounan Mn deposit is proposed as follows.

Mn from the Permian Emeishan basalts, Mn-bearing rocks of Yuebei palaeoisland, and hydrothermal fluid was transported to the epicontinental shallow-marine sedimentary basins in the form of colloid or Mn^{2+} ions. Under a weakly alkaline, weak oxidising condition, Mn^{2+} formed $MnHCO_3^+$ or was oxidised to unstable Mn^{3+}, which then easily formed complex states such as Mn(III)-ligand complexes (Madison et al., 2013) or Mn(III) oxyhydroxides (β-MnOOH and γ-MnOOH) (Hem and Lind, 1983; Murray et al., 1985). The Mn (III)-ligand complexes or oxyhydroxides will interact with silica (H_4SiO_4) to form braunite (Su, 1983; Johnson et al., 2016). Turbulent hydrodynamic conditions in the shallow-marine environment led to large amounts of debris, including feldspar, quartz, and biodetritus, being deposited on the surface of the sediments or suspended near the interface of seawater and sediments. In general, the debris surfaces strongly adsorb Mn hydroxide and the complex anionic group ($MnHCO_3^+$). Moreover, abundant bacteria and microalgae are often attached to these debris particles and continue to grow on them. These microorganisms along with the debris form the original nuclei of oolitic micronodules (Fig. 12a). The morphology of the micronodules is also affected by the shape of the debris. As the colloidal oolitic core grows continuously, it becomes enriched in Mn, Fe, Co, Ni, Cu, Sr, Mo, REEs, and other elements by adsorption, co-precipitation, cation exchange, and the like because the bacteria and algae that form the oolitic core have a strong ability to adsorb metals and non-metallic and complex anionic groups. Furthermore, these biological components can improve the oxidation rate of Mn significantly, and accelerate the accumulation of Mn and the growth of micronodules (Morgan, 1967; Hao and Peng, 1998). In this regard, a

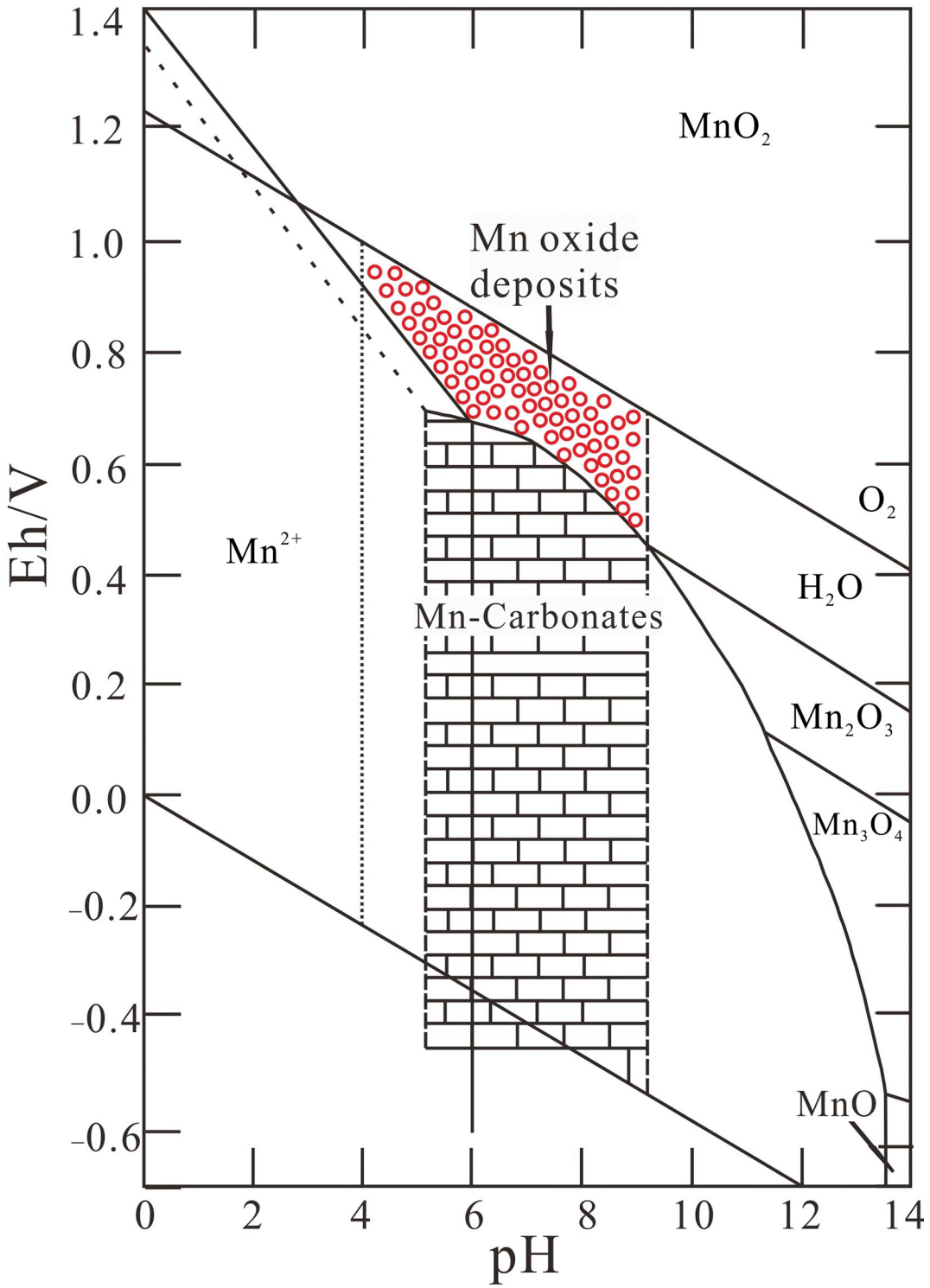

Fig. 11. Stability of Mn oxide and Mn carbonate deposits in natural water. [After Roy, 2006.]

comparison between Co, Ni, and other elements of oceanic Mn nodules and those of the micronodules from the Dounan Mn deposit revealed that the micronodules probably formed by rapid growth (Liu et al., 1984), thus indicating the biological components played a role in the rapid accumulation of Mn.

The original micronodules often have concentric rings with braunite, interbedded with Mn carbonate minerals (Figs. 7a, d; 8; and 9a). The regular stratification of the Mn minerals (with the two main valences mentioned above) shows that the redox condition was a crucial factor in controlling the characteristics of the concentric rings. Studies have shown that the Eh-pH balance of a medium plays a major controlling role in the precipitation form and dissolution of Mn (Krauskopf, 1957; Frakes and Bolton, 1992; Roy, 2006; Fig. 11). The oxygen level of a mineralised water medium is affected by the intensity of the biological activity and organic matter content (Frakes and Bolton, 1992). In an epicontinental basin environment, the organic matter content is abundant and the biological activity is vigorous. The periodic metabolic activity easily causes changes in O_2, CO_2, and other substances in the

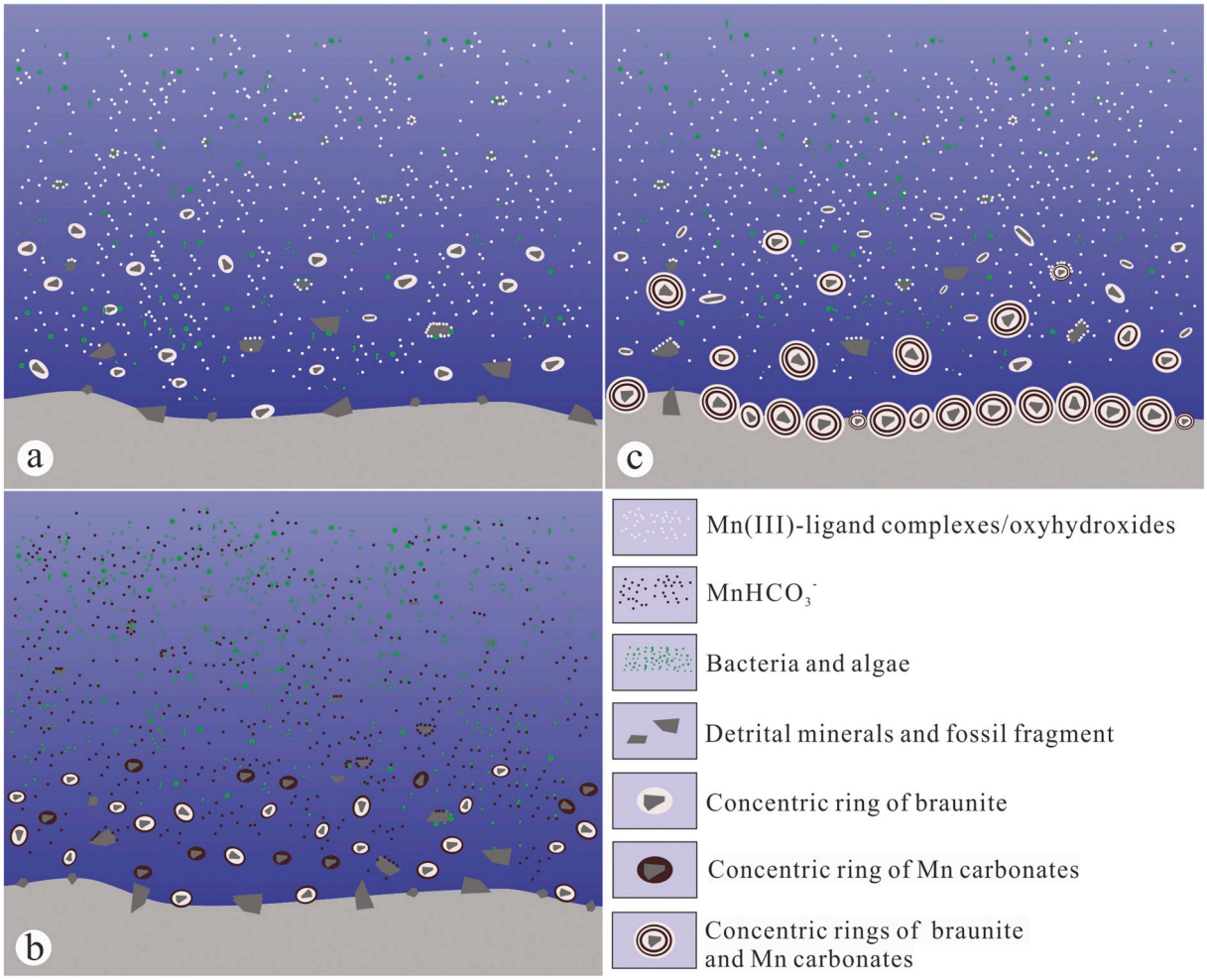

Fig. 12. Schematic diagram of the formation of micronodules near the interface of seawater and sediments in the Dounan Mn deposit.
(a): The formation of primitive oolitic embryos and concentric layer of braunite under the oxidation condition; (b): the formation of concentric layer of manganese carbonates under weakly reducing condition; (c): periodic growth of the two concentric layers.

aquatic environment, thus leading to periodic changes in the Eh and pH of the seawater microenvironment (Su, 1983; Frakes and Bolton, 1992). Therefore, periodic activity of the bacteria and algae could have caused the formation of concentric rings in the micronodules.

In this case, when the oxygen content in the water was high and the aqueous medium was weakly oxidised, free Mn^{2+} oxidised to Mn^{3+} in the metastable state. The original oolitic embryo became enriched in Mn in the form of Mn hydroxide (MnOOH) through biochemical adsorption and ion exchange, and finally, formed braunite layers (Fig. 9b, e; Fig. 12a). Furthermore, the activity of bacteria and algae consumed O_2 in the aqueous medium and released substances such as CO_2, thus causing the redox condition to change from a weak oxidation to a weak reduction state. This stopped the conversion of Mn^{2+} into Mn^{3+}, but Mn complex anions ($MnHCO_3^+$) formed in the weak alkaline condition. At the same time, some of the Mn^{2+} was replaced by Ca^{2+} and Mg^{2+} in the seawater or pore water to form layers composed of Ca-rhodochrosite, kutnahorite, and other Mn carbonate species (Fig. 9c, f; Fig. 12b). Periodic biological activity induced recurrent periodic growth of the two types of layers in the micronodules (Fig. 12c). After growing to a certain size, these micronodules deposited on the surface of the sediments, and possibly, they underwent continuous rolling and growing for a limited period induced by turbulent hydrodynamic conditions. During such episodes, the micronodules adsorbed or replaced the metal ions in the pore water, thus leading to Mn re-enrichment, followed by orderly stacking of the micronodules by a hydrodynamic mechanical sorting effect, and finally, they were buried (Fig. 12c). The Mn minerals in the initial micronodules were colloidal or cryptocrystalline, with poorly developed crystals. The micronodules were not consolidated fully in the buried state, and after compaction, these often developed lenticular or irregular shapes. The three different morphologies of the micronodules described in the previous section demonstrate that they have been transformed by late-stage mineralisation.

6.4. Genesis of the Dounan Mn deposit

Mn is sensitive to the physical and chemical conditions in a depositional environment, particularly the Eh and pH; in different depositional environments, it often forms typical Mn mineral assemblages (Roy, 1988; Roy, 2006; Maynard, 2010). The formation of Mn ore can be divided into four categories according to the different types of Mn minerals and mineralisation (Gutzmer and Beukes, 1996; Johnson et al., 2016). (1) In an oxidative condition, Mn appears in the form of Mn^{4+} oxides, forming birnessite and todorokite through hydrogenous and diagenetic processes, such as in the modern marine Mn nodules. (2) After sedimentation and diagenesis, Mn appears in the form of Mn^{2+} or (and) Mn^{3+}, forming layered and oolitic braunite, Ca-rhodochrosite, kutnahorite, manganocalcite and calcimangite, such as in the Hotazel Formation of the Kalahari Mn field of South Africa. (3) During the late stage of diagenesis, the addition of fluids causes Mn minerals influenced by the hydrothermal effect and metamorphism to form a series of Mn silicate minerals, such as caryopilite, rhodonite, and hausmannite in the Santa Cruz Formation of the Kalahari Mn field. (4) The early formed Mn

minerals can be subjected to surficial weathering, forming cryptomelane and pyrolusite, such as in the superficial Mn nodules in southeast Yunnan, China. In the Dounan Mn deposit, the main Mn mineral assemblages are braunite, Ca-rhodochrosite and small amounts of manganite and calcimangite. The mineral structures are mostly primary sedimentary features, such as oolitic, fine granular, and clastic features, which indicate that the metallogenesis was controlled mainly by sedimentation and diagenesis. Various types of micronodules are commonly developed in the oolitic and pisolitic Mn ores. The change in their morphologies from a complete type to a transitional type to a remnant remodelling type indicates that the Mn ore was subjected to synsedimentary processes and the transformative effect of post-sedimentary diagenesis. Most of the primary Mn minerals are colloidal or cryptocrystalline (Hou, 1994). The morphologies of the octahedral braunite and the hexagonal calcimangite observed by SEM at high magnification (Fig. 8b_1, b_2) indicate that early formed braunite and Mn carbonates experienced recrystallisation. The presence of Mn-bearing calcite veins in the micronodules (Fig. 7d) indicates the addition of hydrothermal fluids during post-depositional stages.

Geochemical information on major and trace elements and REEs are often used to discriminate the genesis of Mn deposits (Shah and Khan, 1999; Öksüz, 2011; Brusnitsyn, 2013). The Mn/Fe ratio is one of the important indexes reflecting the separation degree of Mn and Fe and the ore-forming environment. Under hydrogenetic conditions, the separation between them is not obvious and the Mn/Fe ratio is often less than 1, while under diagenetic or hydrothermal conditions, the separation of Mn and Fe is relatively high, with a higher Mn/Fe ratio (Glasby, 2000). The Mn/Fe ratios of the bulk samples from the Dounan Mn deposit range from 4.95 to 168 (mean 54.7), thus showing characteristics of both diagenetic and hydrothermal Mn deposits (Nicholson et al., 1997; Glasby, 2000; Jach and Dudek, 2005). The (Cu + Ni + Co) × 10–Fe–Mn (wt%) ternary diagram (Bonatti et al., 1972; Crerar et al., 1982) has been used widely to delineate the genesis of Mn deposits. This diagram for the bulk samples and micronodules shows that mineralisation in the study area falls into the overlapping diagenetic and hydrothermal fields (Fig. 13a). The ΣREE content in sedimentary Mn deposits with different geneses varies significantly, with the content of a hydrogenetic Mn deposit being much higher than that of a diagenesis or hydrothermal type, and the REE patterns show a positive Ce anomaly. The REE patterns of hydrothermal Mn deposits have a significant negative Ce anomaly and positive Eu anomaly (Usui et al., 1997; Bau et al., 2014). Fig. 10b shows that the ΣREE contents of the bulk samples and the two micronodules from the Dounan Mn deposit are much lower than those from the hydrogenous Mn ore deposit, mostly falling between diagenetic and hydrothermal. The REE patterns of the bulk samples, BG9JH and GK2JH show that the samples are slightly enriched in heavy REEs (HREEs) and have weakly positive and weakly negative Ce anomalies, as well as a weakly positive Eu anomaly (Tables 1 and 3, Fig. 10b). These REE characteristics suggest that mineralisation in the study area could have been affected by a combination of diagenetic and hydrothermal processes. The discrimination diagram based on Ce/Ce* vs Nd (Bau et al., 2014) indicates that the mineralisation of the Dounan Mn deposit was controlled mainly by sedimentary diagenesis, and the hydrothermal effect had a certain influence on the mineralisation (Fig. 13b).

In addition to the above mineralogical and geochemical analyses, the mineralisation of the Dounan Mn deposit was shown to be dominated by sedimentary diagenesis. Late recrystallisation and the addition of hydrothermal fluids modified the primary Mn minerals and contributed to Mn re-enrichment. The analyses of the micronodules suggest that biogenic processes had a certain influence on the mineralisation. Considering the change rule of the vertical profile of rock (ore), we propose that the mineralisation process of the deposit is as follows:

In the early stage of metallogenesis, terrigenous Mn, transported in the form of colloids or ions and/or Mn^{2+} and liberated by the dissolution of seabed rocks, was transported to the shallow-marine environment at the edge of the basin for the preconcentration stage (Fig. 14a). During the early transgressive, the ore-forming aqueous medium was oxidised weakly; Mn^{2+} was oxidised to Mn^{3+} in a metastable state and first transformed into manganite or bixbyite near the redox interface, and subsequently, it reacted with H_4SiO_4 (aqueous) to eventually generate the braunite layer (Su, 1983; Johnson et al., 2016; Fig. 14b). With the expansion of the transgression, the redox interface rose, which led to the aqueous environment of the primary braunite layer changing into a weakly reduced state. Partial reduction of the primary braunite increased the Mn^{2+} concentration of the pore water, thus causing Mn to fill into the incompletely reduced braunite in the form of carbonate (Tang and Yi, 2011), thereby forming a mixed Mn ore phase that comprised a mixture of braunite and Mn carbonate minerals (Fig. 14c). If the transgression continued to expand until the redox interface rose to the maximum, the Mn^{2+} enriched in the seawater would have continued to precipitate on the original mixed Mn ore layer to form a Mn carbonate layer, and (Fig. 14d) when the Mn could not be replenished in time, a mudstone interlayer formed. Finally, the redox interface decreased as regression occurred, and braunite or a non-ore-bearing interlayer continued to be deposited above the Mn carbonate ore layer. When the development of transgression or regression continued and was slow, these Mn ore layers presented a complete

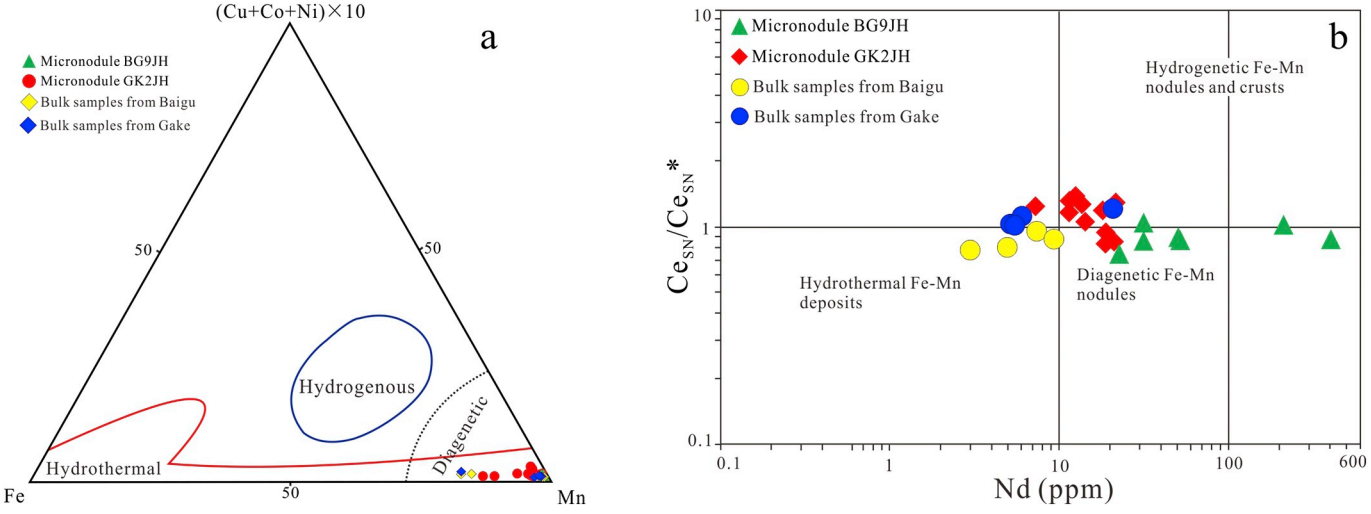

Fig. 13. (a) Discrimination diagram of (Cu + Ni + Co) × 10 (ppm)–Fe–Mn (wt%); (b) plots of discrimination diagrams of Ce_{SN}/Ce_{SN}^* vs Nd concentration for Dounan Mn deposit [discrimination plots after Bau et al., 2014].

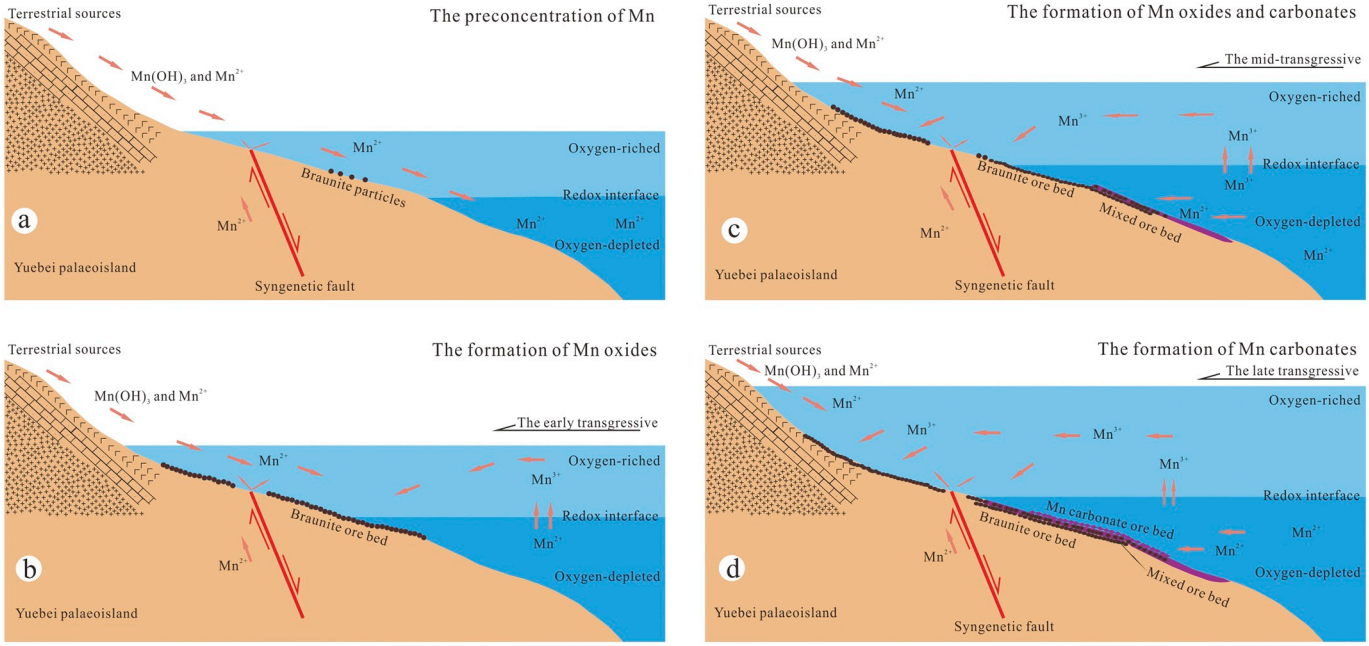

Fig. 14. Schematic diagram of the mineralisation processes in the Dounan Mn deposit.
(a): The stage of the preconcentration of Mn; (b): the stage of braunite formation; (c): the stage of braunite and Mn carbonates formation; (d): the stage of Mn carbonates formation.

transgression–regression sedimentary rhythm cycle. When the development was rapid, or the sedimentary basin uplifted weakly, some of the ore phases were absent. After compaction, early formed Mn ores were subjected to diagenesis and recrystallisation or other changes, thus prompting further enrichment in Mn. Furthermore, hydrothermal activity in the late stage of ore formation occurred and was mainly displayed by the Mn-bearing calcite vein partially replacing and filling into the early formed Mn ores.

7. Conclusions

The Dounan Mn deposit occurs in the Middle Triassic Falang Formation, which comprises a combination of marine mudstone, siltstone, and sandstone interbedded with carbonate rocks. The mineral assemblages are mainly braunite, manganite, Ca-rhodochrosite, calcimangite, and kutnahorite. The metallogenic material was multi-sourced and, mainly derived from the weathering products of the Permian Emeishan basalts and the Mn-bearing rocks of the Yuebei palaeoisland, while some of the Mn was derived from a hydrothermal source. The depositional environment was a shallow marine one with normal salinity, and the slope face was located at the conjunction between the continental margin and the edge of the basin. The physical and chemical conditions of mineralisation were weakly alkaline and fluctuated among oxic, suboxic, and weakly reducing. The formation mechanism of the micronodules involved a combination of chemical and biological processes. Concentric rings in the micronodules were caused by cyclical changes in the formation environment, which were the result of the cyclical activity of microorganisms. The mineralising process of the Dounan Mn ores was dominated by sedimentary diagenesis, and the late stage metallogenesis was affected to some extent by the hydrothermal effect. The formation of the Dounan deposit was controlled by redox interface fluctuations caused by sea level changes.

Declaration of competing interest

This manuscript has not been published or presented elsewhere, and it is not under consideration by another journal. All the authors have approved the manuscript and agree with submission to your esteemed journal. There are no conflicts of interest to declare.

Acknowledgements

The authors are grateful to engineer Chao Li and Lifei Zhu (Yunnan Wenshan Dounan Manganese Industry Co., Ltd.) for their help with collecting field samples. We also thank Wenqin Zheng, Zhihui Dai, Jing Hu, Shaohua Dong, Shuqin Yang and Yong Meng for their help with the analyses of the study. This research was financially supported by the National Key R&D Program of China (2018YFC0603505), the National Natural Science Foundation of China (No. 41376080, 41703051), the 12th Five-Year Plan project of the State Key Laboratory of Ore Deposit Geochemistry, Chinese Academy of Sciences (SKLODG-ZY125-08), and the PhD Research Startup Fund Project of East China University of Technology (DHBK2018034).

References

Anschutz, P., Dedieu, K., Desmazes, F., Chaillou, G., 2005. Speciation, oxidation state, and reactivity of particulate manganese in marine sediments. Chem. Geol. 218, 265–327.
Bathurst, R.G.C., 1975. Carbonate Sediments and their Diagenesis. Elsevier, Amsterdam (658 pp).
Bau, M., Dulski, P., 1999. Comparing yttrium and rare earths in hydrothermal fluids from the Mid-Atlantic Ridge: implications for Y and REE behavior during near-vent mixing and for the Y/Ho ratio of Proterozoic seawater. Chem. Geol. 155, 77–90.
Bau, M., Koschinsky, A., Dulski, P., Hein, J.R., 1996. Comparison of the partitioning behaviours of yttrium, rare earth elements, and titanium between hydrogenetic marine ferromanganese crusts and seawater. Geochim. Cosmochim. Acta 60, 1709–1725.
Bau, M., Möller, P., Dulski, P., 1997. Yttrium and lanthanides in eastern Mediterranean seawater and their fractionation during redox-cycling. Mar. Chem. 56, 123–131.
Bau, M., Schmidt, K., Koschinsky, A., Hein, J., Kuhn, T., Usui, A., 2014. Discriminating between different genetic types of marine ferro-manganese crusts and nodules based on rare earth elements and yttrium. Chem. Geol. 381, 1–9.
Bolton, B.R., 1988. Petrography and orign of inversely graded manganese pisolite from Grooteeyland, Australia. Ore Geol. Rev. 4, 47–69.
Bolton, B.R., Frakes, L.A., 1985. Geology and genesis of manganese oolite, Chiatura, Georgia, U.S.S.R. Geol. Soc. Am. Bull. 96 (11), 1398–1406.
Bonatti, E., Kraemer, T., Rydell, H., 1972. Classification and genesis of submarine iron-manganese deposits. In: Horn, D. (Ed.), Ferromanganese Deposits on the Ocean Floor: International Decade of Ocean Exploration. National Science Foundation, Washington, DC, pp. 149–166.
Brusnitsyn, A.I., 2013. Geochemistry and genetic model of the ore-bearing sediments of

the Parnok ferromanganese Deposit, Polar Urals. Geochem. Int. 51 (8), 623–645.
Burkhalter, R.M., 1995. Ooidal ironstones and ferruginous microbialites: origin and relation to sequence stratigraphy (Aalenian and Bajocian, Swiss Jura mountains). Sedimentology 42, 57–74.
Chauvel, J.J., 1974. Les minerais de fer de l'Ordovicien inferieur du bassin de Bretagne, Anjou, France. Sedimentology 21, 127–147.
Chukhrov, F.V., Gorshkov, A.I., Beresovskaya, V.V., Sivtsov, A.V., 1979. Contributions to the mineralogy of authigenic manganese phases from marine manganese deposits. Mineral., Deposita (Berl.) I4, 249–261.
Crerar, D.A., Namson, J., Chyi, M.S., Williams, L., Feigenson, M.D., 1982. Manganiferous cherts of the Franciscan assemblage: I. General geology, ancient and modern analogues, and implications for the hydrothermal convection at oceanic spreading centers. Econ. Geol. 77, 519–540.
Du, Q.D., Yi, H.S., Hui, B., Li, S.J., Xia, G.Q., Yang, W., Wu, X.F., 2013. Recognition, genesis and evolution of manganese ore deposits in southeastern China. Ore Geol. Rev. 55, 99–109.
Duan, J.B., Fu, Y.Z., Zhang, Z.W., Ma, X.X., Xiao, J.F., 2019. The metallogenic environment of the Dounan manganese deposit, Southeast Yunnan, China: evidence from geochemistry and Mössbauer spectroscopic. Acta Geochimica 38 (1), 78–94.
Ehrlich, H.L., 1980. Different forms of microbial manganese oxidation and reduction and their environmental significance. In: Trudinger, P.A., Walter, M.R., Ralph, B.J. (Eds.), Biogeochemistry of Ancient and Modern Environments. Australian Academy of Science, Canberra, pp. 327–332.
Fan, D.L., Yang, P.J., 1999. Introduce to and classification of manganese deposits of China. Ore Geol. Rev. 15, 1–15.
Frakes and Bolton, 1992. Effects of ocean chemistry, sea level, and climate on the formation of primary sedimentary manganese ore deposits. Econ. Geol. 87 (5), 1207–1217.
Frakes, L.A., Bolton, B.R., 1984. Origin of manganese giants: sea-level change and anoxic-oxic history. Geology 12 (2), 83–86.
Garnit, H., Bouhlel, S., 2017. Petrography, mineralogy and geochemistry of the Late Eocene oolitic ironstones of the Jebel Ank, Southern Tunisian Atlas. Ore Geol. Rev. 84, 134–153.
Glasby, G.P., 2000. Manganese: predominant role of nodules and crusts. Marine Geochemistry 371 (3), 371–427.
Guo, L.G., 2006. Primary Reaserch on Geochemistry and Geochronology of the Laojunshan Metamorphic Core Complex, Southeastern Yunnan. University of Chinese Academy of Sciences, Beijing, China (in Chinese with English abstract).
Gutzmer, J., Beukes, N.J., 1996. Mineral paragenesis of the Kalahari manganese field, South Africa. Ore Geol. Rev. 11, 405–428.
Hao, H.X., Peng, L.S., 1998. Microbial geochemistry of manganese. Bull. Mineral. Petrol. Geochem. 17 (3), 197–200 (in Chinese).
Hayashi, K., Fujisawa, H., Holland, H., Ohmoto, H., 1997. Geochemistry of 1.9 Ga Sedimentary Rocksfrom Northeastern Labrador, Canada. Geochim. Cosmochim. Acta 61, 4115–4137.
Hein, J.R., Koschinsky, A., Halbach, P., Manheim, F.T., Bau, M., Kang, J.K., Lubick, N., 1997. Iron and manganese oxide mineralization in the Pacific. In: Nicholson, K., Hein, J.R., Buhn, B., Dasgupta, S. (Eds.), Manganese Mineralization: Geochemistry and Mineralogy of Terrestrial and Marine Deposits. Geological Society Special Publication 119. pp. 123–138.
Hein, J.R., Mizell, K., Koschinsky, A., Conrad, T.A., 2013. Deep-ocean mineral deposits as a source of critical metals for high- and green-technology applications: comparison with land-based resources. Ore Geol. Rev. 51, 1–14.
Hem, J.D., Lind, C.J., 1983. Nonequilibrium models for predicting forms of precipitated manganese oxides. Geochim. Cosmochim. Acta 47, 2037–2046.
Henderson, P., 1984. Rare Earth Element Geochemistry. Elsevier, Amsterdam.
Hou, B.H., 1994. Primary braunite in Triassic sedimentary manganese deposits of Dounan, Yunnan, China. Ore Geol. Rev. 9, 219–239.
Hou, Z.L., Xue, Y.Z., Huang, J.S., Lin, Y.H., Liu, H.J., Yao, J.Q., Zhu, K.J., 1997. Manganese Ore in the Peripheral Area of Yangtze Platform. Metallurgy Industry Press, Beijing.
Hu, X.Y., 2009. Determine the major element concentrations of carbonate rocks using X-ray fluorescence spectrometry. Acta Mineral. Sin. 598 (S), 597 (in Chinese).
Huang, J.S., Zhu, K.J., Wang, S.B., Zhu, Z.S., 1996. Outline of marine Mn deposit in the South China. Contr Geol Miner Resour Res 11 (3), 9–17 (in Chinese with English abstract).
Jach, R., Dudek, T., 2005. Origin of a Toarcian manganese carbonate/silicate deposit from the Krížna unit, Tatra Mountains, Poland. Chem. Geol. 224, 136–152.
Janin, M.C., Bignot, G., 1983. Thallophytic microfossils of the laminated polymetallic concretions. Micropalaeontology 25, 251–264.
Ji, X.X., Zhou, S., Chen, Q., et al., 2016. Provenance and tectonic setting of the Kunyang Group in central Yunnan Province. Geol. China 43 (3), 857–878 (in Chinese with English abstract).
Johnson, J.E., Webb, S.M., Ma, C., Fischer, W.W., 2016. Manganese mineralogy and diagenesis in the sedimentary rock record. Geochim. Cosmochim. Acta 173, 210–231.
Krauskopf, K.B., 1957. Separation of manganese from iron in semdimentary process. Geochim. Cosmochim. Acta 2, 61–84.
Krauskopf, K.B., 1979. Introduction to Geochemistry. McGraw Hill, New York.
Krumbein, W.E., 1983. Stromatolites: the challenge of a term in space and time. Precambrian Res. 20, 493–531.
Li, S.J., Yi, H.S., Ma, X., Xia, G.Q., Rong, J.F., Da, X.J., 2009. Sedimentary facies of the manganese-bearing strata in the Falang Formation, southeastern Yunnan. Sediment. Geol. Tethyan Geol. 29 (2), 33–38 (in Chinese with English abstract).
Liu, H.J., Xue, Y.Z., 1999. Sedimentology of Triassic Dounan-type manganese deposits, western margin, Yangtze Platform, China. Ore Geol. Rev. 15, 165–176.
Liu, et al., 1984. Typical deposit research report of Dounan manganese deposits, Yanshan County, Yunnan Province. Geol. Miner. Bur. Yunnan Province 1–106 (in Chinese).
Liu, R.F., Tian, B.K., Shi, Z.Z., Hao, R.X., Li, H.C., 1988. Geochemical characteristics of the Mn bearing-Falang formation in the Southeast Yunnan Province. Contributions To Geology and Mineral Resources Research 3 (4), 1–19 (in Chinese with English abstract).
Liu, R.F., Tian, B.K., Shi, Z.Z., Hao, R.X., Li, H.C., 1989. Mn-nodule in the southeast Yunnan Province. Contributions To Geology and Mineral Resources Research 4 (3), 58–66 (in Chinese with English abstract).
Liu, Y.S., Hu, Z.C., Gao, S., Günther, D., Xu, J., Gao, C.G., Chen, H.H., 2008. In situ analysis of major and trace elements of anhydrous minerals by LA-ICP-MS without applying an internal standard. Chem. Geol. 257, 34–43.
Macquaker, J.H.S., Taylor, K.G., Young, T.P., Curtis, C.D., 1996. Sedimentological and geochemical controls on ooidal ironstone and "bone-bed" formation and some comments on their sequence stratigraphical significance. In: Hesselbo, S., Parkinson, D.N. (Eds.), Sequence Stratigraphy in British Geology. 103. Geol. Soc. Spec. Publ, pp. 97–107.
Madison, A.S., Tebo, B.M., Mucci, A., Sundby, B., Luther, G.W., 2013. Abundant porewater Mn(III) is a major component of the sedimentary redox system. Science 341, 875–878.
Maynard, J., 2010. The chemistry of manganese ores through time: a signal of increasing diversity of earth-surface environments. Econ. Geol. 105, 535–552.
McLennan, S.M., 1989. Rare earth elements in sedimentary rocks: influence of provenance and sedimentary processes. In: Lipin, B.R., McKay, G.A. (Eds.), Geochemistry and Mineralogy of Rare Earth Elements. Mineral. Soc. Am, pp. 169–200.
Morgan, J.J., 1967. Chemical equilibria and kinetic properties of manganese in natural waters. In: Faust, S.D., Hunter, J.V. (Eds.), Principles and Applications of Water Chemistry. Wiley, pp. 561–620.
Murray, J.W., Dillard, J.G., Giovanoli, R., Moers, H., Stumm, W., 1985. Oxidation of Mn (II): initial mineralogy, oxidation state and ageing. Geochim. Cosmochim. Acta 49, 463–470.
Nath, B.B., Pluger, W.L., Roelandts, I., 1997. Geochemical constraints on thehydrothermal origin of ferromanganese incrustations from the Rodriguez triple junction, Indian Ocean. In: Nicholson, K., Hein, J.R., Bühn, B., Dasgupta, S. (Eds.), Manganese Mineralization: Geochemistry and Mineralogy of Terrestrial and Marine Deposits. 119. Geol. Soci. Lond. Spec. Publ, pp. 199–211.
Nicholson, K., Nayak, V.K., Nanda, J.K., 1997. Manganese ores of the Ghoriajhor-Monmunda area, Sundergarh District, Orissa, India: geochemical evidence for a mixed Mn source. Geol. Soc. Lond. Spec. Publ. 119, 117–121.
Öksüz, N., 2011. Geochemical characteristics of the Eymir (Sorgun-Yozgat) manganese deposits, Turkey. J. Rare Earths 29 (3), 287–296.
Öksüz, N., Okuyucu, N., 2014. Mineralogy, geochemistry, and origin of Buyukmahal manganese mineralization in the Artova Ophiolitic Complex, Yozgat, Turkey. Journal of Chemistry 1–11.
Ostwald, J., 1990. The biogeochemical origin of the Groote Eylandt manganese oxide pisoliths and ooliths, northern Australia. Ore Geol. Rev. 5 (5), 469–490.
Pack, A., Russell, S.S., Shelley, J.M.G., et al., 2007. Geo-and cosmochemistry of the twin elements yttrium and holmium. Geochim. Cosmochim. Acta 71, 4592–4608.
Peng, D., Lin, L., Wang, Q.W., Kan, Z.Zh., Fu, X.F., Peng, B., 2011. The discovery of manganese nodules in Garze-Litang suture zone. Geol. China 38 (2), 442–450.
Qi, L., Hu, J.D., Conrad, G., 2000a. Determination of trace elements in granites by inductively coupled plasma mass spectrometry. Talanta 51 (3), 507–513.
Qi, L., Hu, J.D., Xu, D.Y., 2000b. Determination of rare earth elements and trace elements in manganese concretion by laser ablation-inductively coupled plasma mass spectrometry. Chinese Journal of Analysis Laboratory 19 (4), 56–59.
Roy, S., 1988. Manganese metallogenesis: a review. Ore Geol. Rev. 4, 155–170.
Roy, S., 2006. Sedimentary manganese metallogenesis in response to the evolution of the Earth system. Earth Sci. Rev. 77, 273–305.
Salama, W., Aref, M.E., Gaupp, R., 2012. Mineralogical and geochemical investigations of the Middle Eocene ironstones, El Bahariya Depression, Western Desert, Egypt. Gondwana Res. 22, 717–736.
Shah, M.T., Khan, A., 1999. Geochemistry and origin of Mn-deposits in the Waziristan ophiolite complex, north Waziristan, Pakistan. Mineral. Deposita 34, 697–704.
Song, X., 1989. Metallogenic epochs and distribution of China's Mn-deposits. Geology and Prospecting 25 (5), 3–10 (in Chinese with English abstract).
Stumm, W., Morgan, J.J., 1996. Aquatic Chemistry, 3rd ed. J. Wiley and Sons, New York.
Su, J.H., 1983. Dounan manganese doposit: a braunite deposit of sedimentary origin. Bulletin of the Institute of Mineral Deposits, Chinese Academy of Geological Sciences. 4, 3–49 (in Chinese with English abstract).
Sugahara, H., Sugitani, K., Mimura, K., et al., 2010. A systematic rare-earth elements and yttrium study of Archean cherts at the Mount Goldsworthy greenstone belt in the Pilbara Craton: implication for the origin of microfossil-bearing black cherts. Precambrian Res. 177, 73–87.
Sugisaki, R., 1984. Relation between chemical composition and sedimentation rate of Pacific Ocean floor sediments deposited since the middle Cretaceous: basic evidence for chemical constraints on depsitional environments of ancient sediments. The Journal of Geology 92, 235–259.
Surya Prakash, L., Ray, D., Paropkari, A.L., Mudholkar, A.V., Satyanarayanan, M., Sreenivas, B., Chandrasekharam, D., Kota, D., Raju, K.A.K., Kaisary, S., Balaram, V., Gurav, T., 2012. Distribution of REEs and yttrium among major geochemical phases of marine Fe–Mn-oxides: comparative study between hydrogenous and hydrothermal deposits. Chem. Geol. 312–313, 127–137.
Tan, W.F., Liu, F., Li, Y.H., He, J.Z., Li, X.Y., 2000. Mineralogy of manganese in iron-manganese nodules of several soils in China. Acta Pedol. Sin. 37 (2), 192–201 (in Chinese with English abstract).
Tang, Y.F., Yi, H.S., 2011. Mineral phase changes and depositional model of sedimentary manganese deposits in Dounan area of southeastern Yunnan. Geol. China 38 (2),

451–461 (in Chinese with English abstract).
Taylor, S.R., McLennan, S.M., 1985. The continental crust: its composition and evolution. An examination of the geochemical record preserved in sedimentary rocks. Blackwell Scientific Publishing, Oxford.
Toyoda, K., Masuda, A., 1990. Sedimentary enviroments and chemical composition of Pacific pelagic sediments. Chem. Geol. 88, 127–141.
Usui, A., Someya, M., 1997. Distribution and composition of marine hydrogenetic and hydrothermal manganese deposits in the northwest Pacific. In: Nicholson, K., Hein, J.R., Buhn, B., Dasgupta, S. (Eds.), Manganese Mineralization: Geochemistry and Mineralogy of Terrestrial and Marine Deposits. 119. Geological Society Special Publication, pp. 177–198.
Van Houten, F.B., Arthur, M.A., 1989. Temporal patterns among Phanerozoic oolitic ironstones and oceanic anoxia. In: Young, T.P., Taylor, W.E.G. (Eds.), Phanerozoic Ironstones: An Introduction and Review. Geological Society of London, London, pp. 33–49.
Wang, F., 2012. Petrology and Metamorphic Mrtamorphic Evolution of the Diancanshan-Ailaoshan Metamorphic Comliex Belt, Southeastern Tibetan Plateau. PhD dissertation. Chinese Academy of Geological Science, China (in Chinese with English abstract).
Wang, Y., Zhou, M.F., Qi, L., 2007. Permian flood basalts and mafic intrusions in the Jinping (SW China)–Song Da (northern Vietnam) district: mantle sources, crustal contamination and sulfide segregation. Chem. Geol. 243, 317–343.
Wegorzewski, A.V., Kuhn, T., 2014. The influence of suboxic diagenesis on the formation of manganese nodules in the Clarion Clipperton nodule belt of the Pacific Ocean. Mar. Geol. 357, 123–138.
Wu, Y.L., Zhu, H.F., el, al., 1994. Triassic Lithofacies Palaeogeography and Mineralization in Southern China. Geological Publishing House, Beijing, China, pp. 99–103.
Xia, G.Q., Yi, H.S., Li, S.J., Wu, X.F., 2010. Research on manganese - accumulation features in Middle Triassic Ladinian sedimentary system and sequence stratigraphic framework, Southeastern Yunnan. Geological Review 56 (5), 703–709 (in Chinese with English abstract).
Yang, Y.M., 2003. Study on Geoehemistry of Fe-Cu-REE Deposit in Kunyang Group in Mid-Proterozoic—Exampled by the Yinachang Fe-Cu-REE Deposit. PhD dissertation. Chinese Academy of Scienee, China (in Chinese with English abstract).
Young, T.P., 1989a. Phanerozoic ironstones: an introduction and review. In: Young, T.P., Taylor, W.E.G. (Eds.), Phanerozoic Ironstones. 46. Geol. Soc. Spec. Publ, pp. 9–25.
Young, T.P., 1989b. Eustatically controlled ooidal ironstone deposition: facies relationships of the Ordovician open shelf ironstones of Western Europe. In: Young, T.P., Taylor, W.E.G. (Eds.), Phanerozoic Ironstones. 46. Geol. Soc. Spec. Publ, pp. 51–63.
Zheng, R.C., Zhang, J.Q., 1991. Gravity flow manganese deposits and their sedimentary environments in Middle Triassic from Dounan, Southeast Yunnan. Chengdu Coll. Geol. 18 (4), 65–75 (in Chinese).
Zhong, J.T., 1986. Metallogeny of the Dounan manganese deposit. Geological Review 32 (6), 583–588 (in Chinese with English abstract).
Zhu, X.K., Peng, Q.Y., Zhang, R.B., An, Z.Z., Zhang, F.F., Yan, B., Li, J., Gao, Z.F., Tan, Y., Pan, W., 2013. Geological and geochemical characteristics of the Daotuo super-large manganese ore deposit at Songtao County in Guizhou Province. Acta Geol. Sin. 87 (9), 1335–1348 (in Chinese with English abstract).